

Supplement to

Particulate matter triggers the formation of extracellular amyloid β and tau- containing plaques and neurite shortening *in vitro*

Aleksandar Sebastijanovič^{1,3} aleksandar.sebastijanovic@infinite-biotech.com

Rok Podlipec^{2,3} r.podlipec@hzdr.de

Alessandra Gianoncelli⁴ alessandra.gianoncelli@elettra.eu

Gregor Hlawacek² g.hlawacek@hzdr.de

Valentina Bonanni⁴ valentina.bonanni@elettra.eu

Laura Maria Azzurra Camassa⁵ Laura.Camassa@stami.no

Vilhelm Malmberg^{6,7,8} vilhelm.malmberg@design.lth.se

Slavko Kralj⁹ slavko.kralj@ijs.si

Joakim Pagels^{7,8} joakim.pagels@design.lth.se

Ulla Vogel⁶ UBV@nfa.dk

Shan Zienolddiny-Narui⁵ shan.narui@stami.no

Iztok Urbančič³ * iztok.urbancic@ijs.si

Tilen Koklič³ * tilen.koklic@ijs.si

Janez Štrancar^{1,3} * janez.strancar@infinite-biotech.com

* To whom correspondence should be addressed

¹ Infinite LLC, Zagrebška cesta 20, 2000 Maribor, Slovenia

² Helmholtz-Zentrum Dresden-Rossendorf e.V., Ion Beam Center, Bautzner Landstrasse 400, 01328 Dresden, Germany

³ Laboratory of Biophysics, Condensed Matter Physics department, Jožef Stefan Institute, Jamova cesta 39, Slovenia

⁴ Elettra, Sincrotrone Trieste, Strada Statale 14 - km 163,5 in AREA Science Park, Trieste, Italy

⁵ National Institute of Occupational Health, Oslo, Norway

⁶ National Research Centre for the Working Environment, DK-2100 Copenhagen, Denmark

⁷ Ergonomics and Aerosol Technology, Lund University, SE-22100 Lund, Sweden

⁸ NanoLund, Lund University, 22100 Lund, Sweden

⁹ Material Synthesis Department, Jožef Stefan Institute, Jamova cesta 39, Slovenia

Contents

1	Nanomaterial aggregation in cell medium	3
2	Fluorescent labelling	21
3	Microscope setup	21
3.1	Main article FIGURE 1 supplementary material	23
4	TiO ₂ nanotubes are present in the extracellular plaques, together with metal ions	27
4.1	Synchrotron micro-XRF.....	29
5	Main article FIGURE 3 supplementary material	30
6	Main article FIGURE 4 supplementary material	30
7	Dose relevance	50
7.1	the amount of nanoparticles found in the brain of Alzheimer’s disease patients	50
7.2	Estimate of the transport of nanoparticle to the brain	51
7.2.1	Traversal through the blood-brain barrier	51
7.2.2	Transport along the olfactory nerve.....	51
7.2.3	Rapid accumulation of nanoparticles in the olfactory bulb:	52
7.2.4	Delayed accumulation of nanoparticles in the deep brain structures:	52
7.3	References	55

1 Nanomaterial aggregation in cell medium

In the following images, we show the aggregation state of each material when suspended in the cell media. Each image represents measurements that were made on different days.

maghemite $\gamma\text{-Fe}_2\text{O}_3$

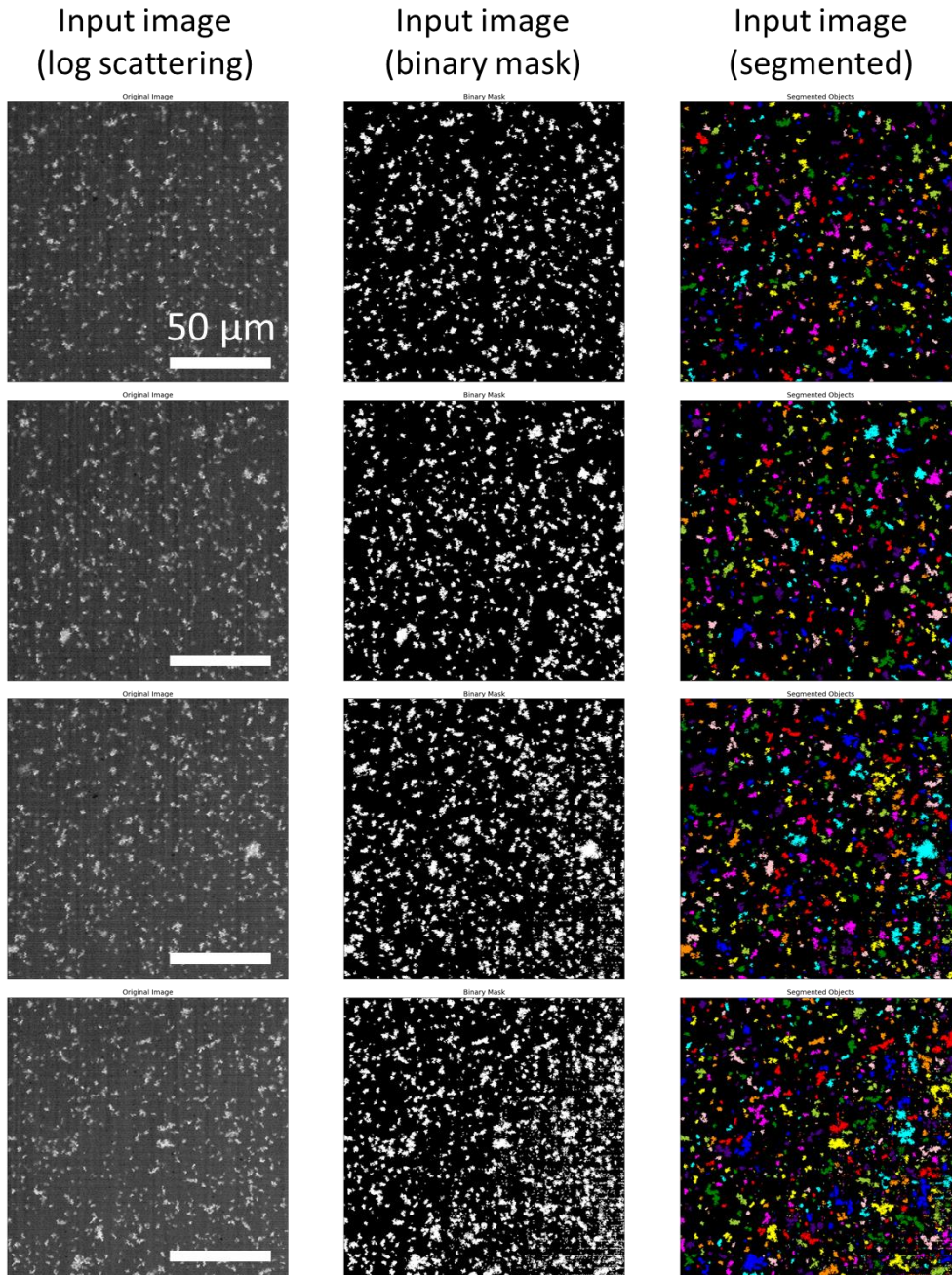


Figure S 1: Log-transformed backscattered signal of 3 μl of maghemite $\gamma\text{-Fe}_2\text{O}_3$ resuspended in the neuronal DMEM/F-12 media. Imaged with the 60X magnification objective after overnight incubation to allow all the material to deposit.

maghemite $\gamma\text{-Fe}_2\text{O}_3$

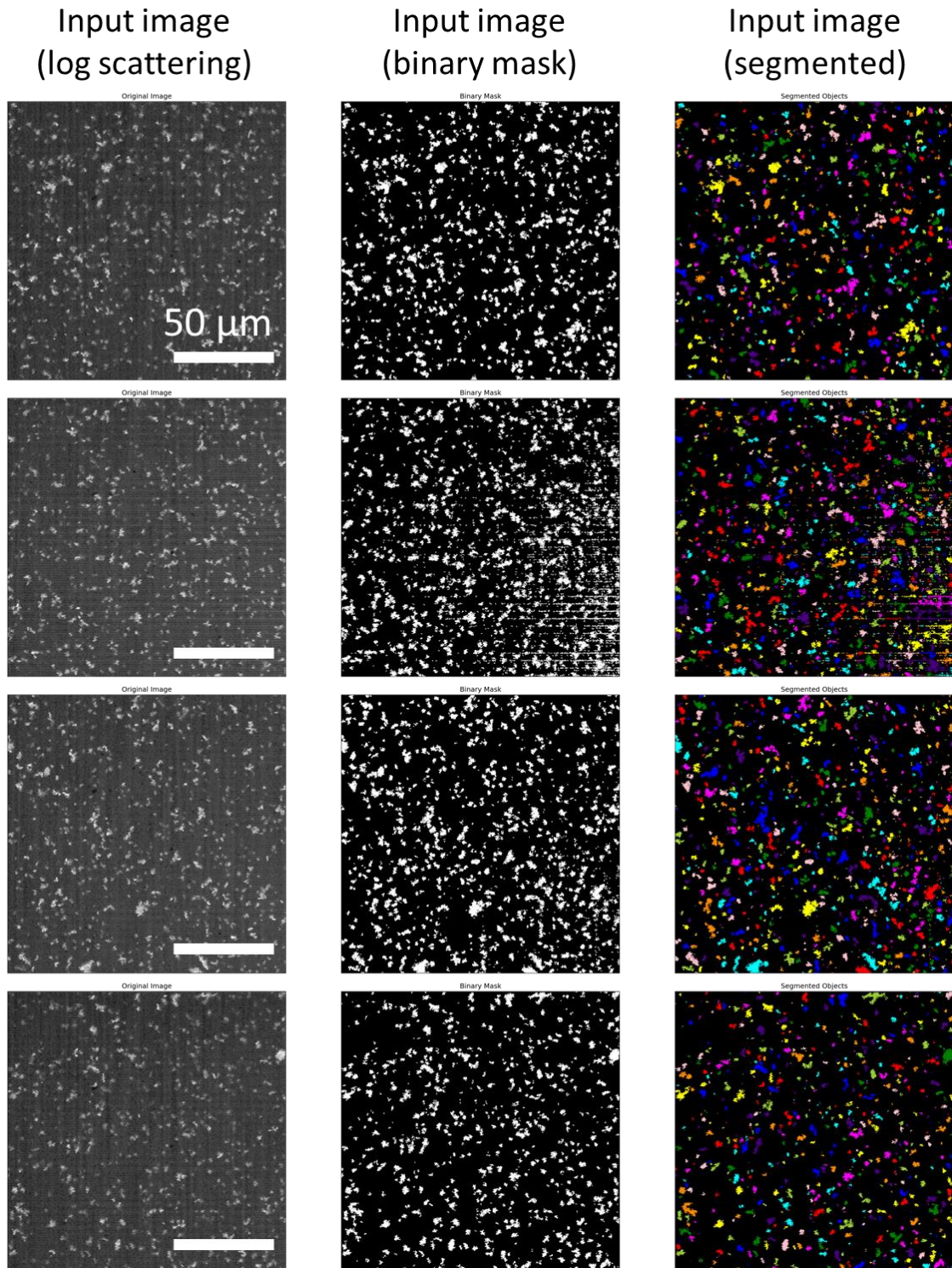
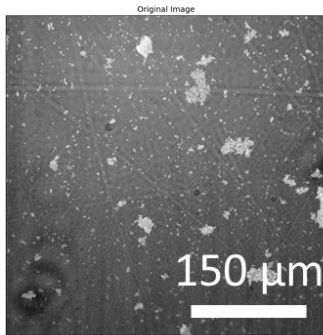


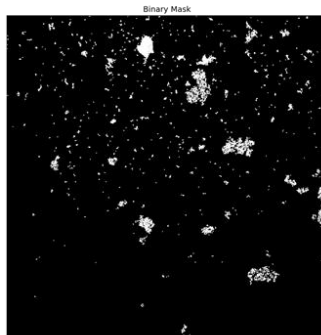
Figure S 2: Log-transformed backscattered signal of 3 μl of maghemite $\gamma\text{-Fe}_2\text{O}_3$ resuspended in the neuronal DMEM/F-12 media. Imaged with the 60X magnification objective after overnight incubation to allow all the material to deposit.

maghemite $\gamma\text{-Fe}_2\text{O}_3$

Input image
(log scattering)



Input image
(binary mask)



Input image
(segmented)

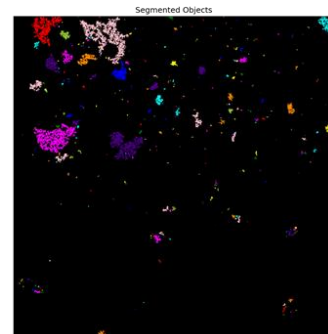
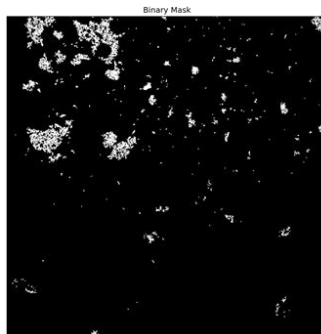
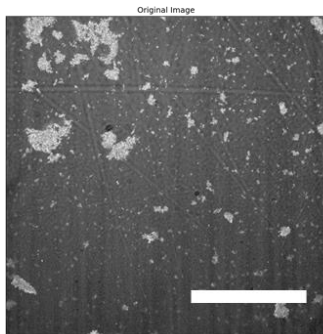
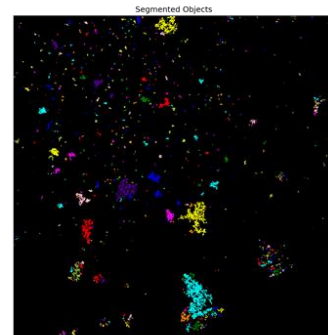
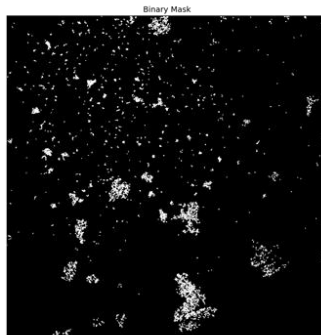
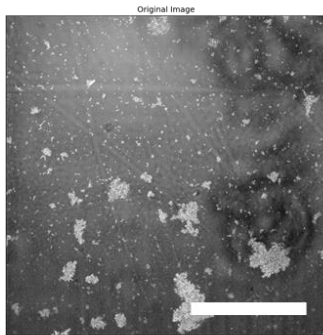
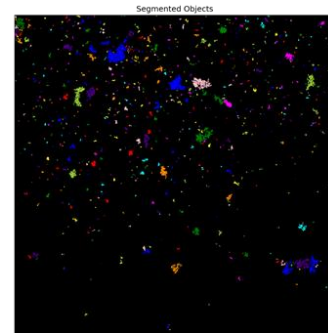
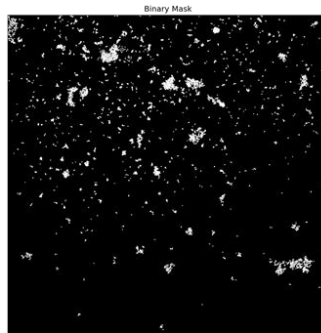
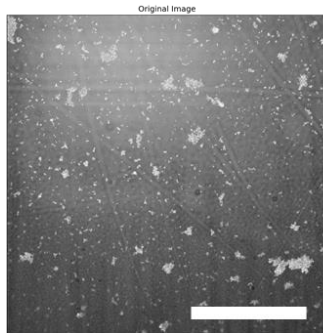
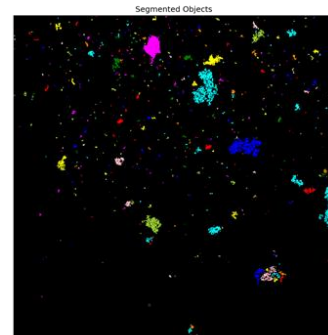


Figure S 3: Log-transformed backscattered signal of 3 μl of maghemite $\gamma\text{-Fe}_2\text{O}_3$ resuspended in the neuronal DMEM/F-12 media. Imaged with the 20X magnification objective after overnight incubation to allow all the material to deposit.

TiO₂

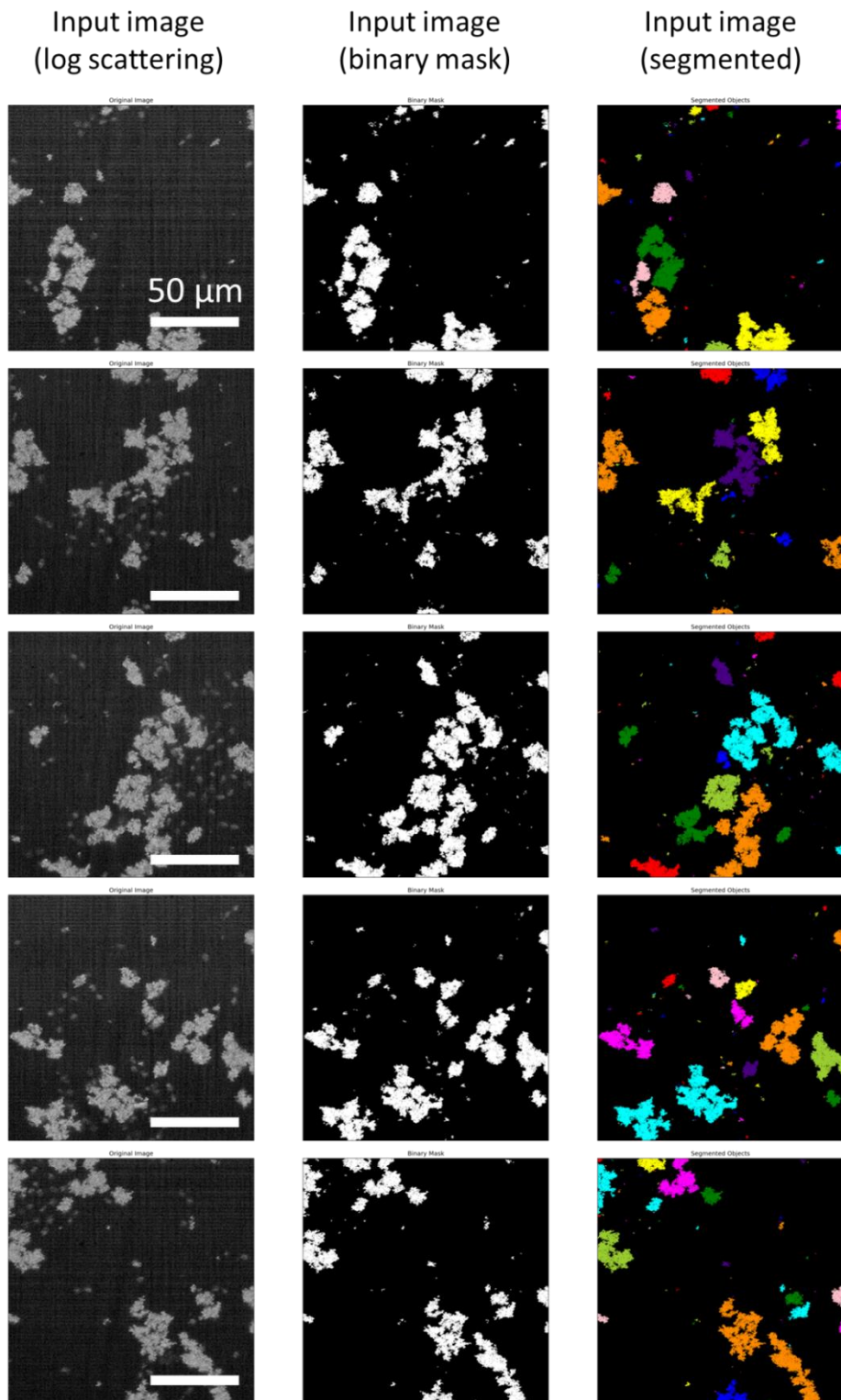
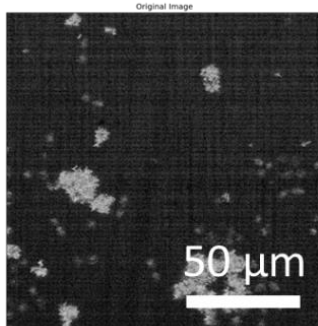


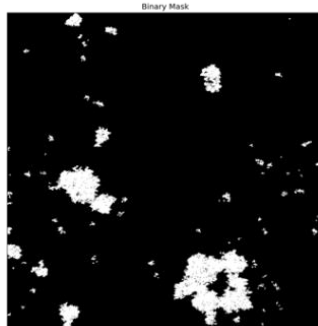
Figure S 4: Log-transformed backscattered signal of 3 μ l of TiO₂ resuspended in the neuronal DMEM/F-12 media. Imaged with the 60X magnification objective after overnight incubation to allow all the material to deposit.

TiO₂

Input image
(log scattering)



Input image
(binary mask)



Input image
(segmented)

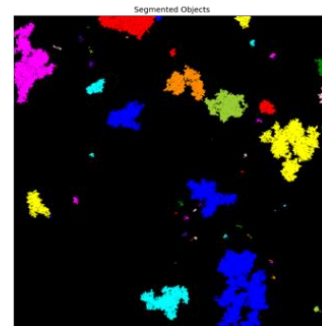
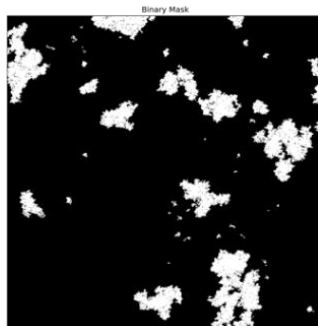
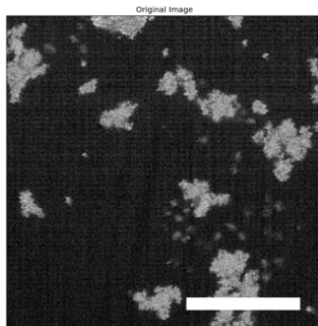
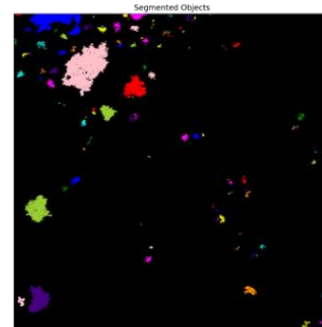
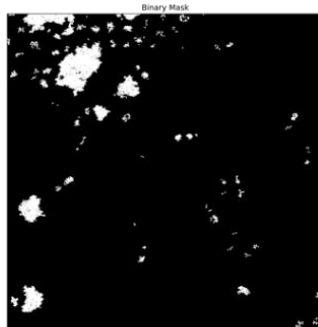
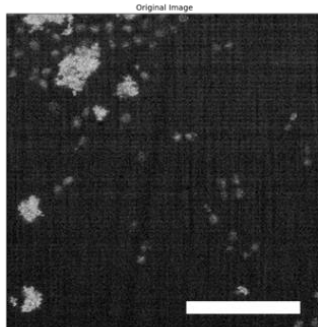
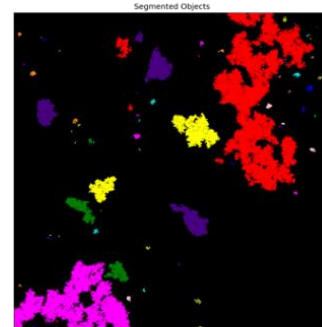
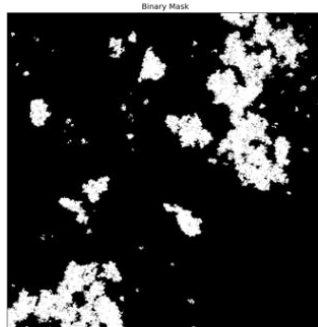
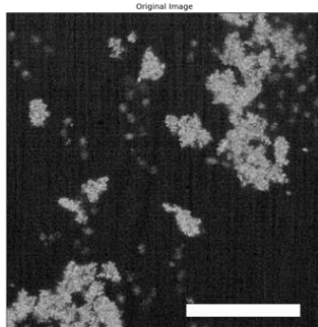
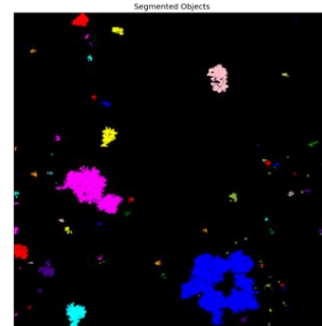


Figure S 5: Log-transformed backscattered signal of 3 μl of TiO₂ resuspended in the neuronal DMEM/F-12 media. Imaged with the 60X magnification objective after overnight incubation to allow all the material to deposit.

TiO₂

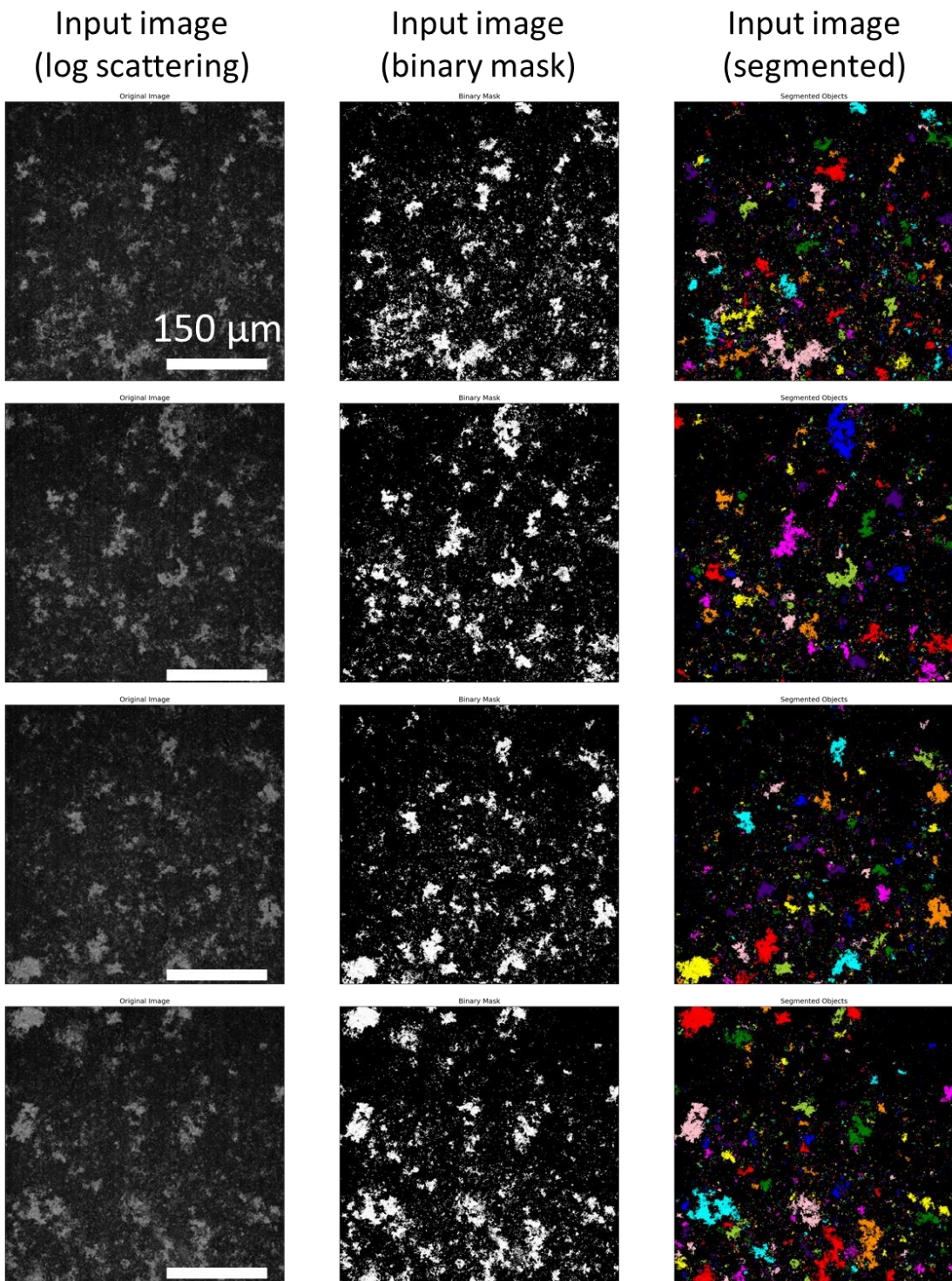
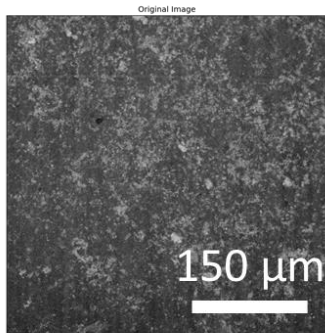


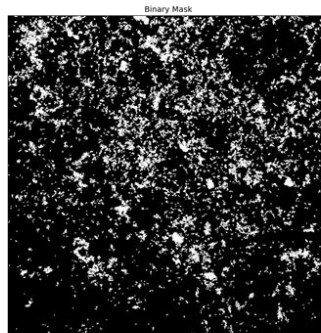
Figure S 6: Log-transformed backscattered signal of 3 μ l of TiO₂ resuspended in the neuronal DMEM/F-12 media. Imaged with the 20X magnification objective after overnight incubation to allow all the material to deposit.

TiO₂

Input image
(log scattering)



Input image
(binary mask)



Input image
(segmented)

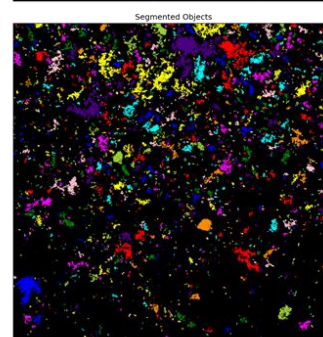
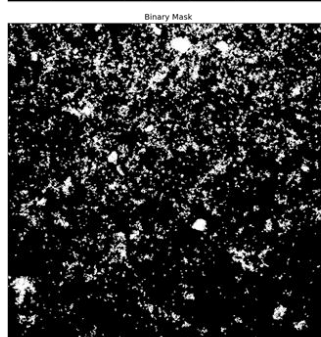
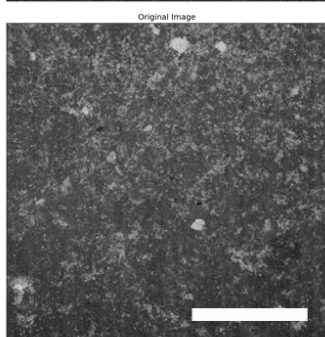
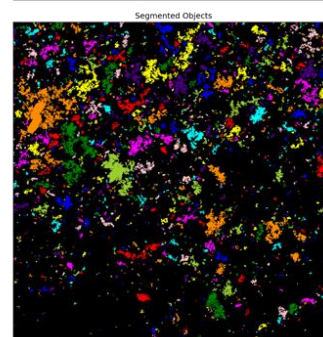
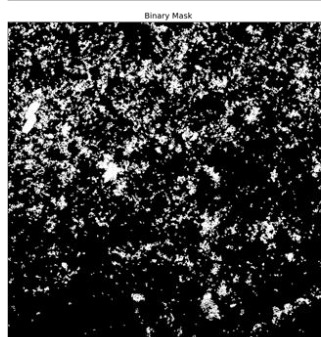
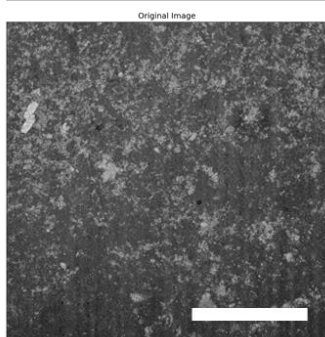
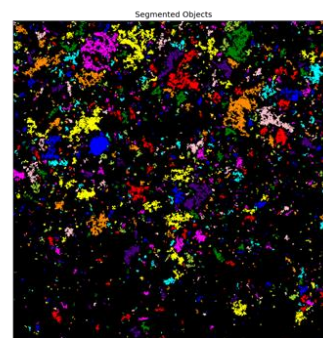
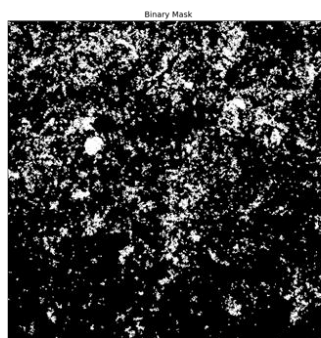
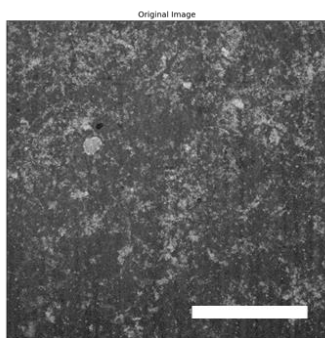
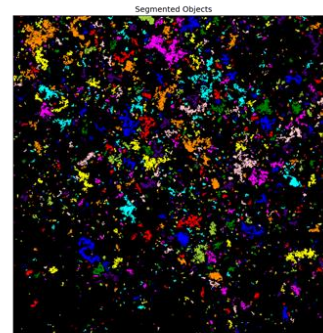


Figure S 7: Log-transformed backscattered signal of 3 μl of TiO₂ resuspended in the neuronal DMEM/F-12 media. Imaged with the 20X magnification objective after overnight incubation to allow all the material to deposit.

CeO₂

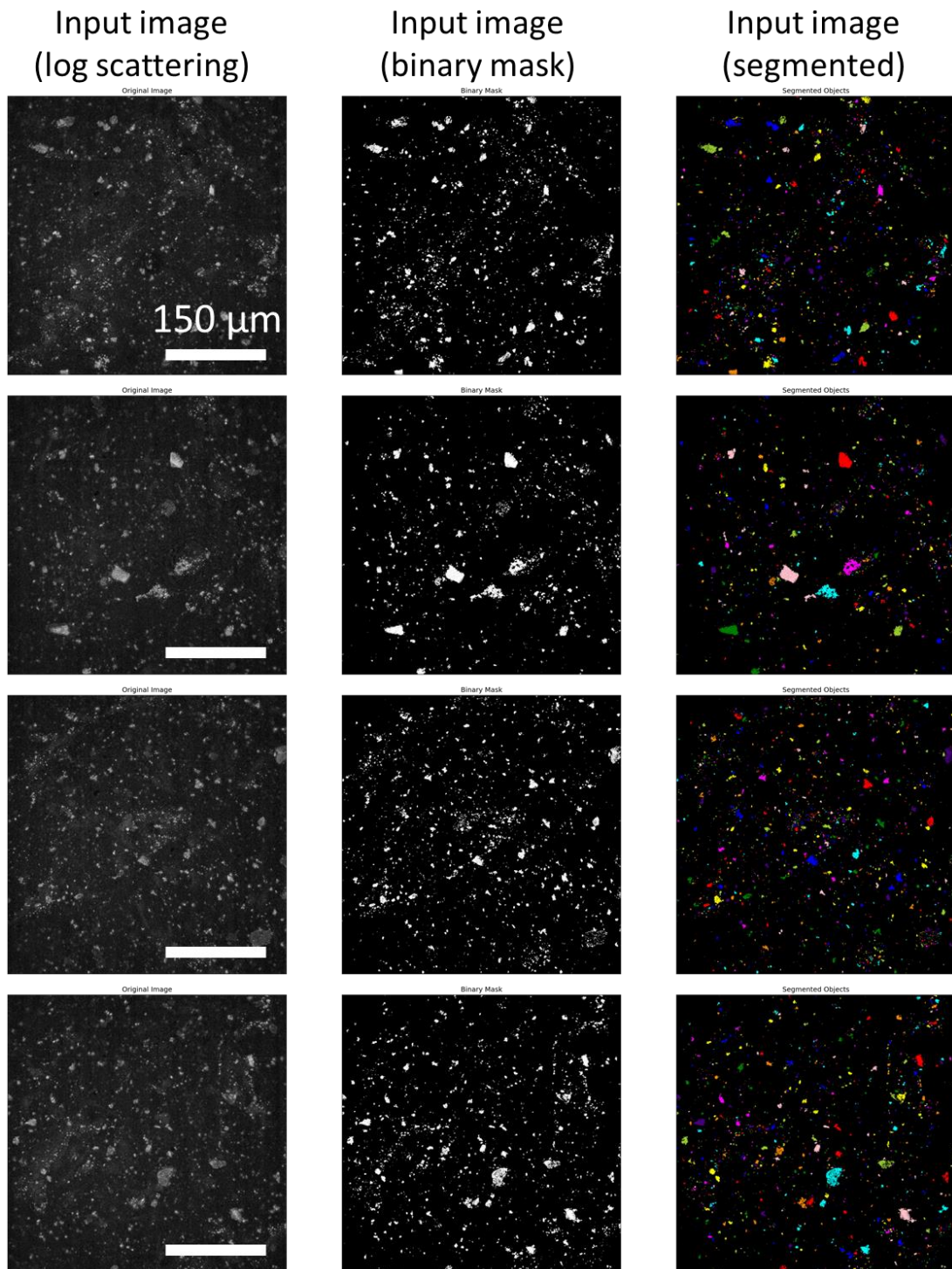


Figure S 8: Log-transformed backscattered signal of 3 μl of CeO₂ resuspended in the neuronal DMEM/F-12 media. Imaged with the 20X magnification objective after overnight incubation to allow all the material to deposit.

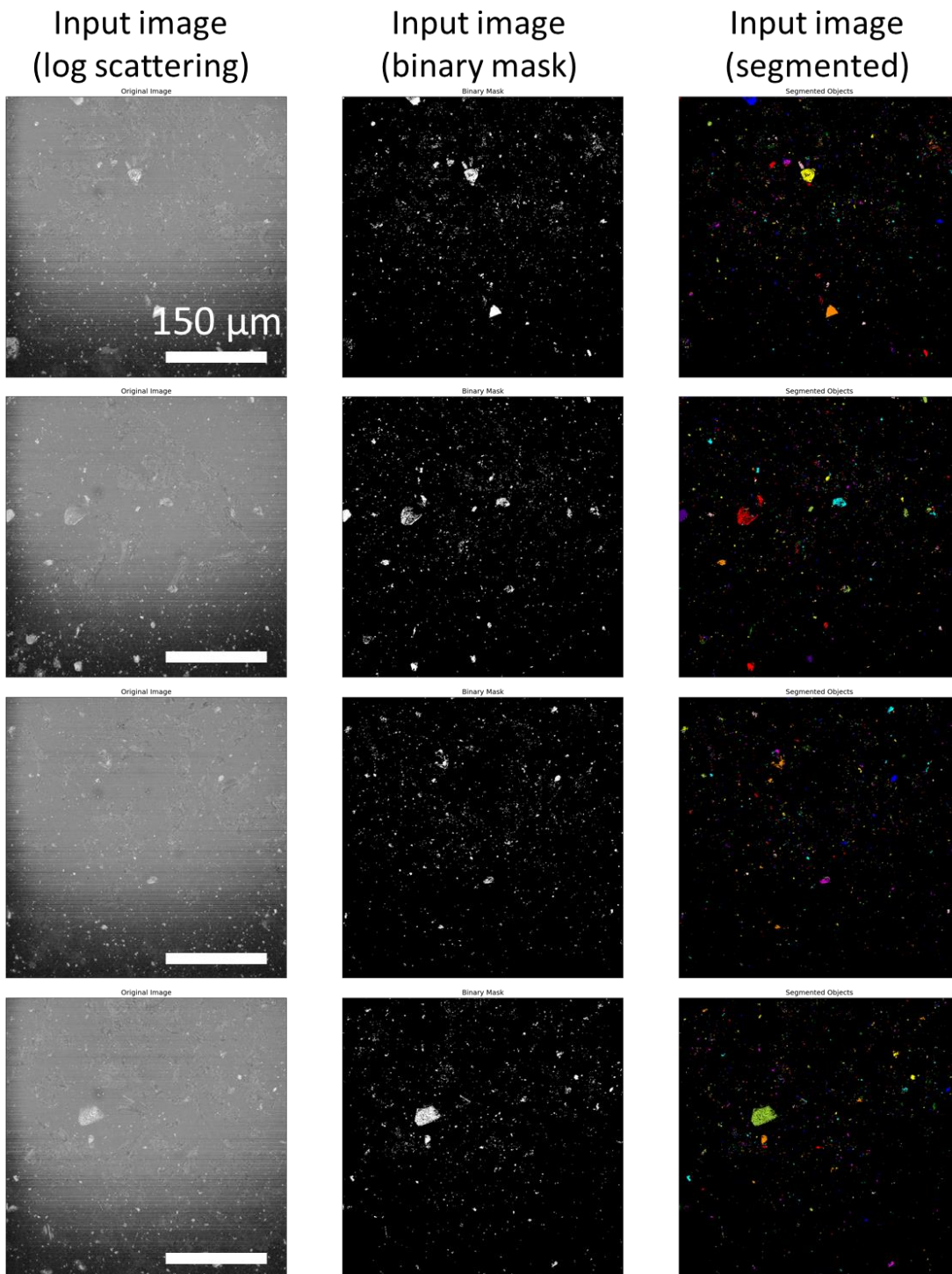


Figure S 9: Log-transformed backscattered signal of 3 μl of CeO₂ resuspended in the neuronal DMEM/F-12 media. Imaged with the 20X magnification objective after overnight incubation to allow all the material to deposit.

CeO₂

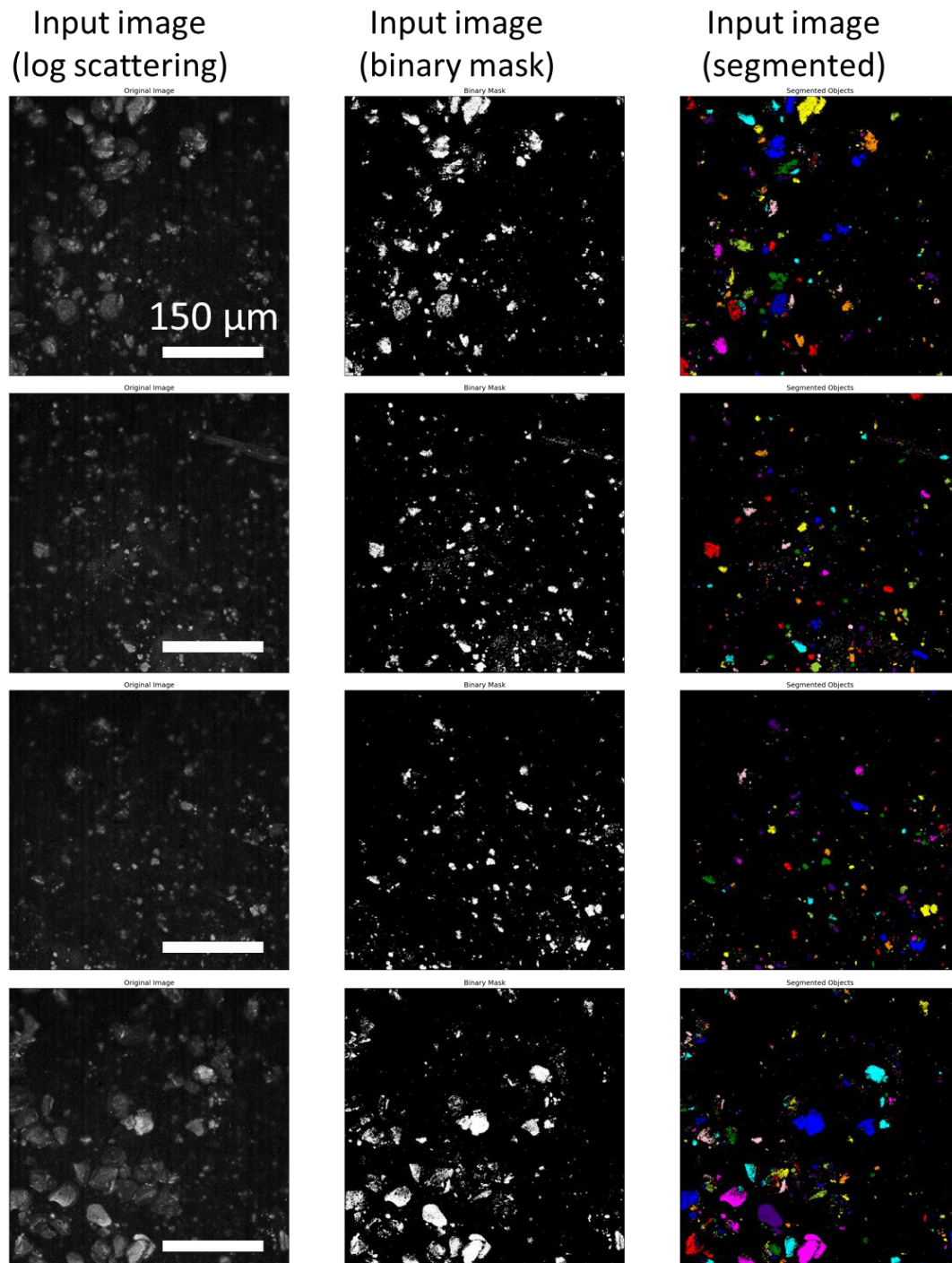


Figure S 10: Log-transformed backscattered signal of 3 μl of CeO₂ resuspended in the neuronal DMEM/F-12 media. Imaged with the 20X magnification objective after overnight incubation to allow all the material to deposit.

Diesel

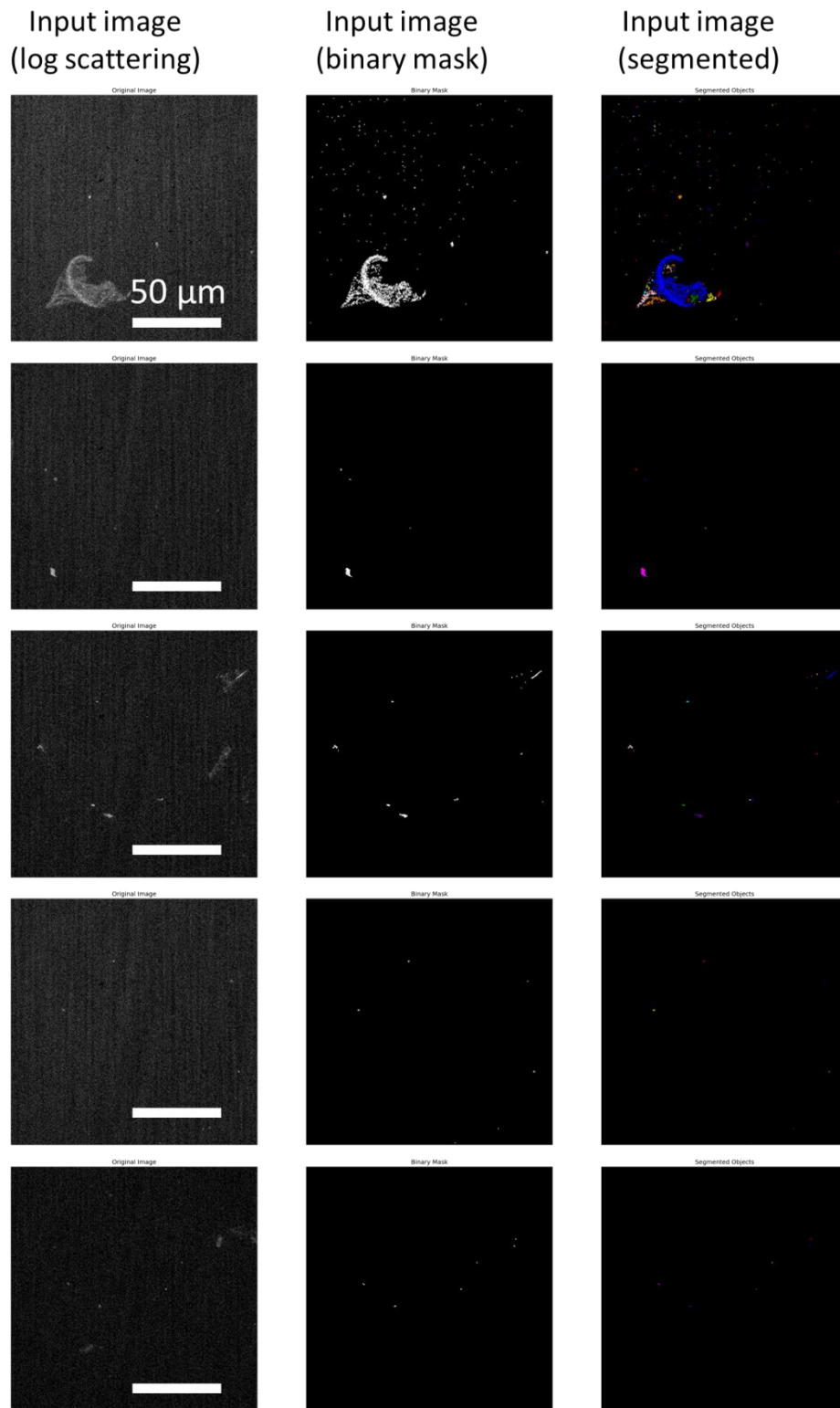


Figure S 11: Log-transformed backscattered signal of 3 μ l of Diesel resuspended in the neuronal DMEM/F-12 media. Imaged with the 60X magnification objective after overnight incubation to allow all the material to deposit.

Diesel

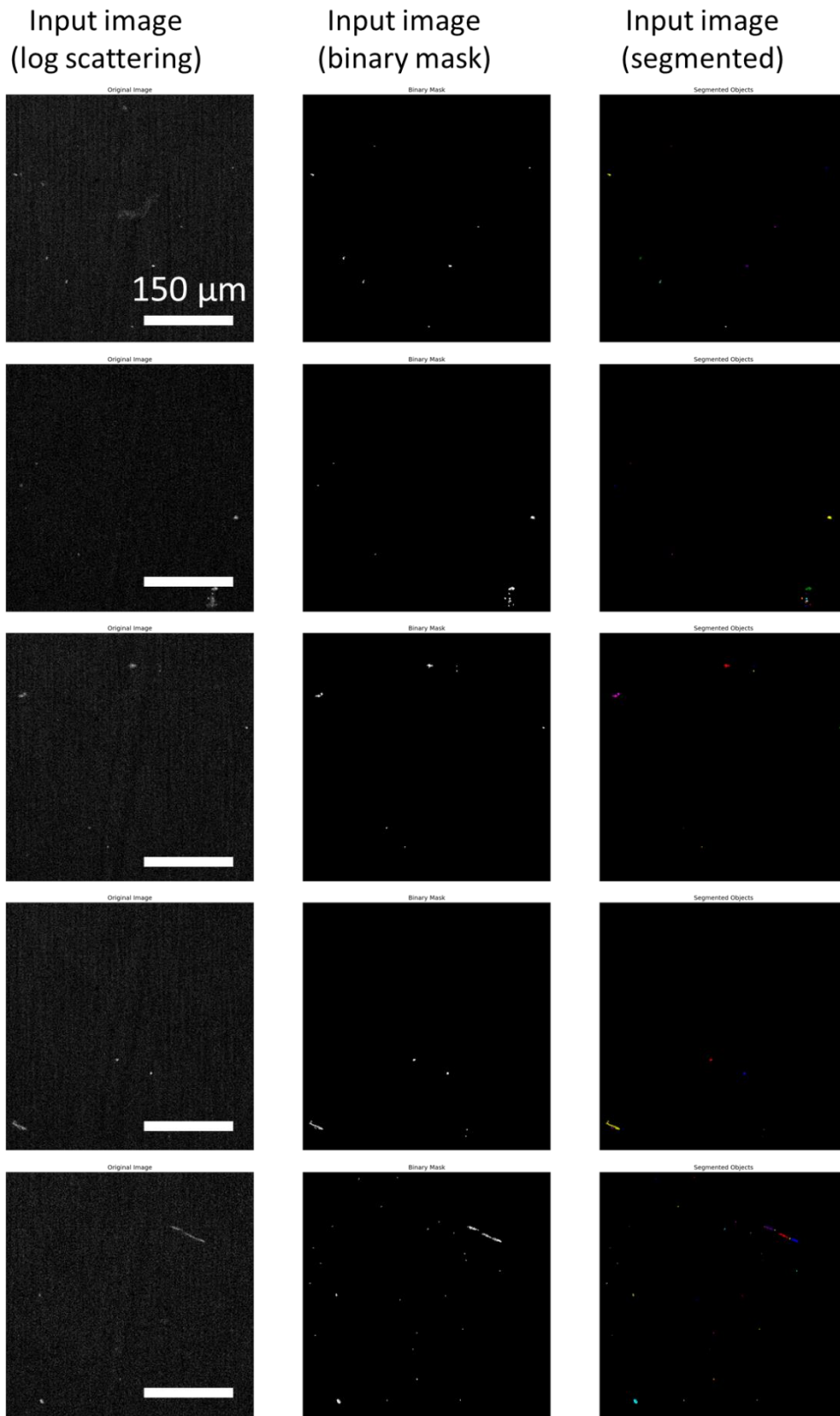


Figure S 12: Log-transformed backscattered signal of 3 μ l of Diesel resuspended in the neuronal DMEM/F-12 media. Imaged with the 20X magnification objective after overnight incubation to allow all the material to deposit.

Diesel

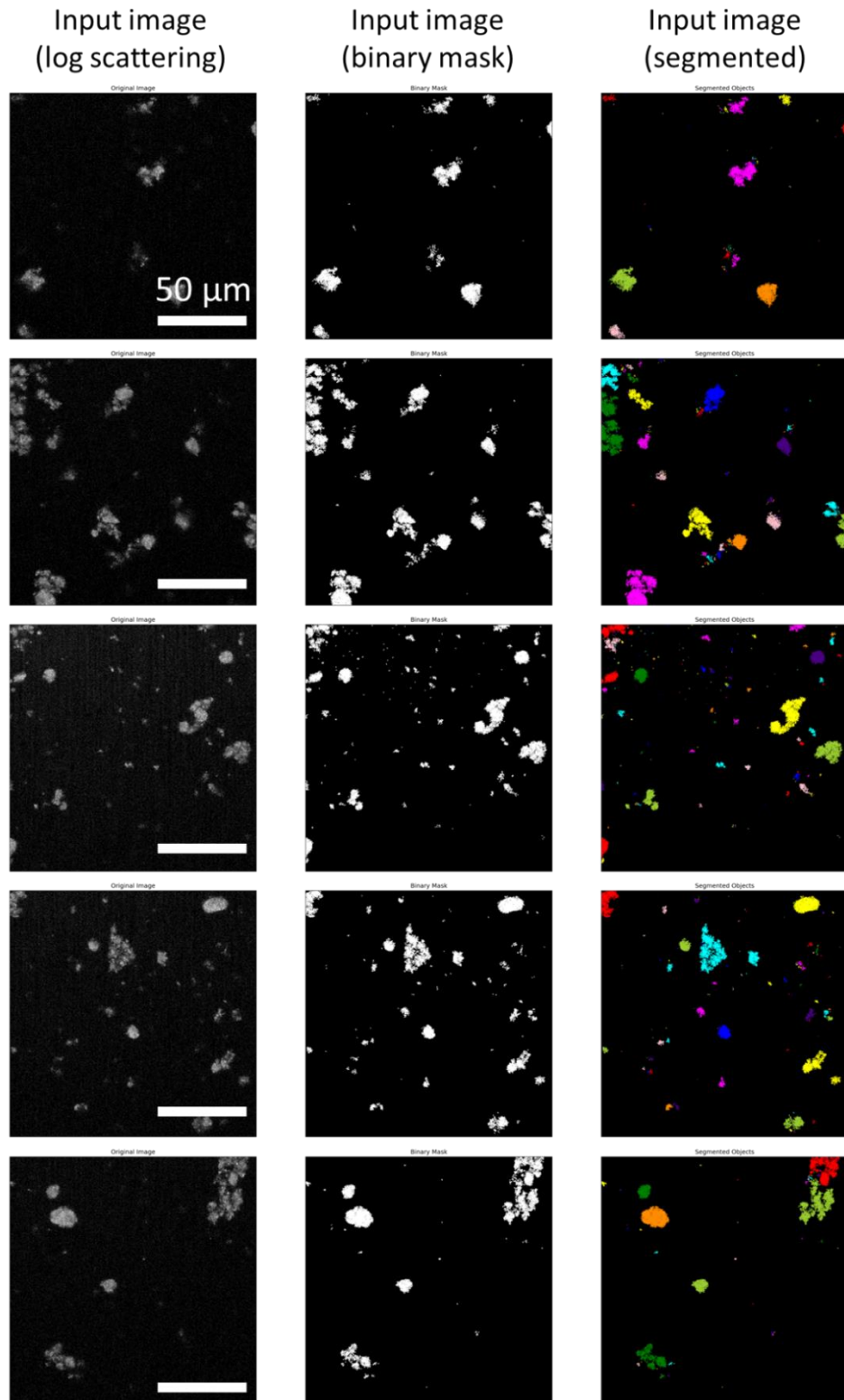


Figure S 13: Log-transformed backscattered signal of 3 μl of Diesel resuspended in the neuronal DMEM/F-12 media. Imaged with the 60X magnification objective after overnight incubation to allow all the material to deposit.

Diesel

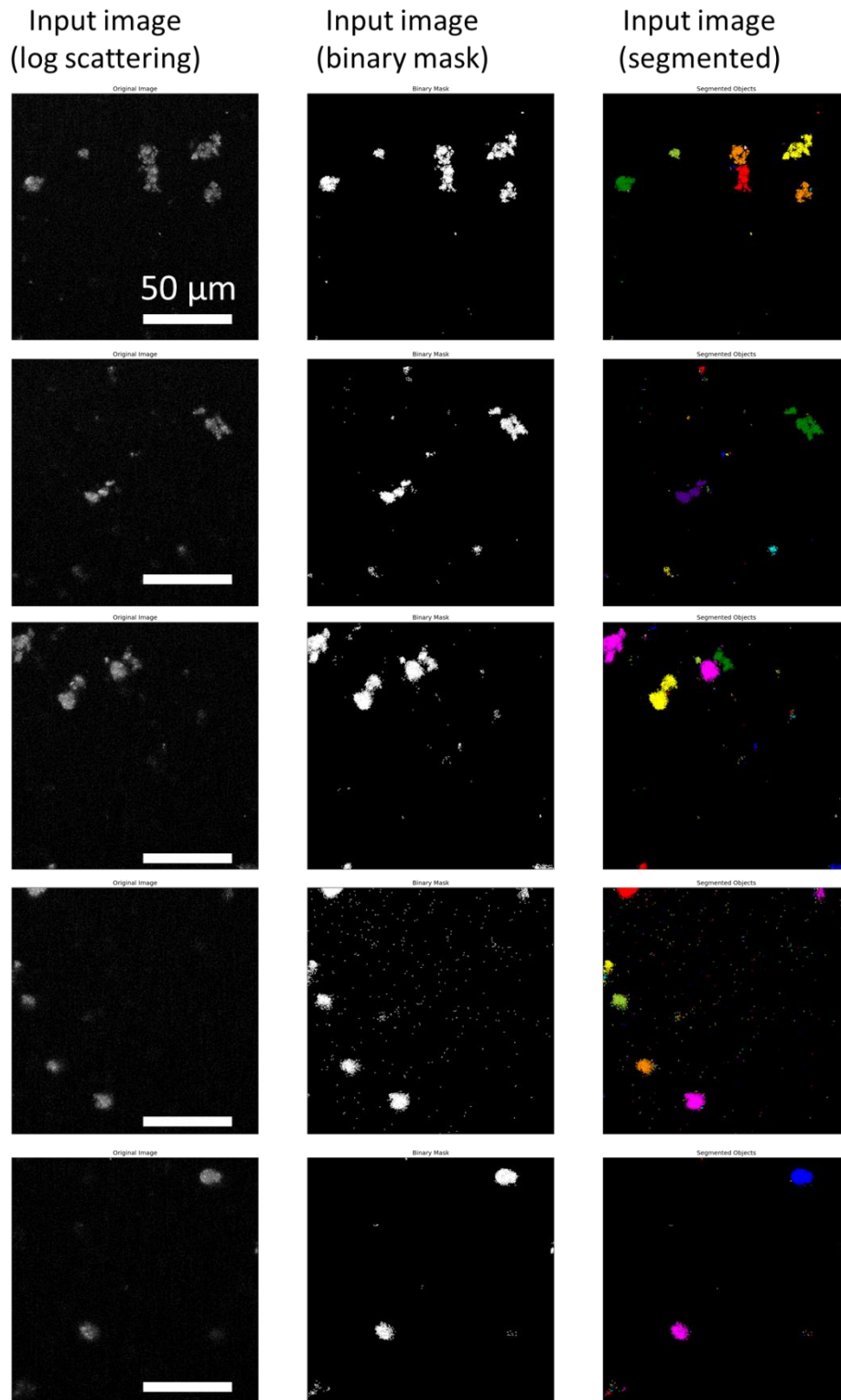


Figure S 14: Log-transformed backscattered signal of 3 μl of Diesel resuspended in the neuronal DMEM/F-12 media. Imaged with the 60X magnification objective after overnight incubation to allow all the material to deposit.

Diesel

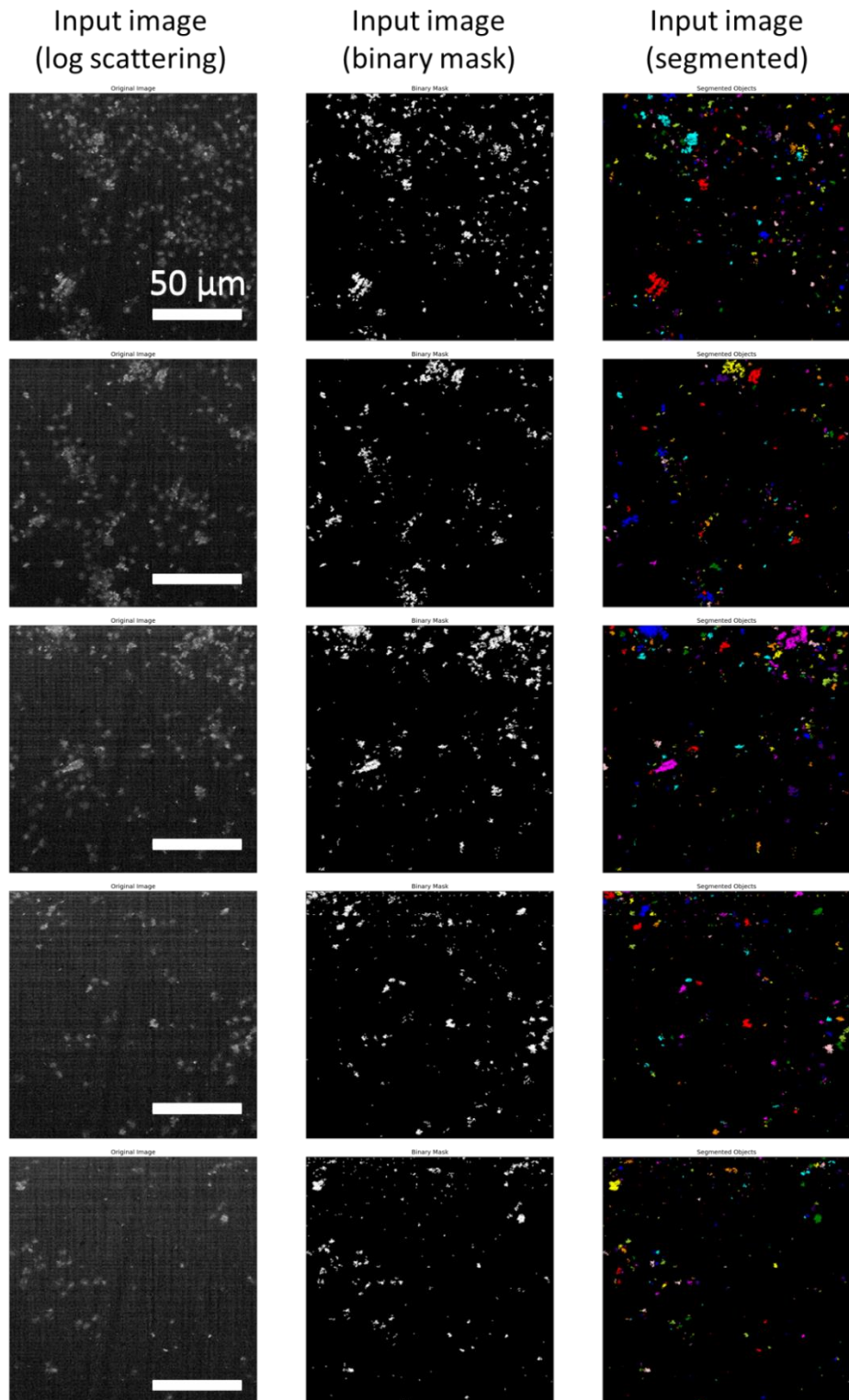


Figure S 15: Log-transformed backscattered signal of 3 μ l of Diesel resuspended in the neuronal DMEM/F-12 media. Imaged with the 60X magnification objective after overnight incubation to allow all the material to deposit.

Diesel

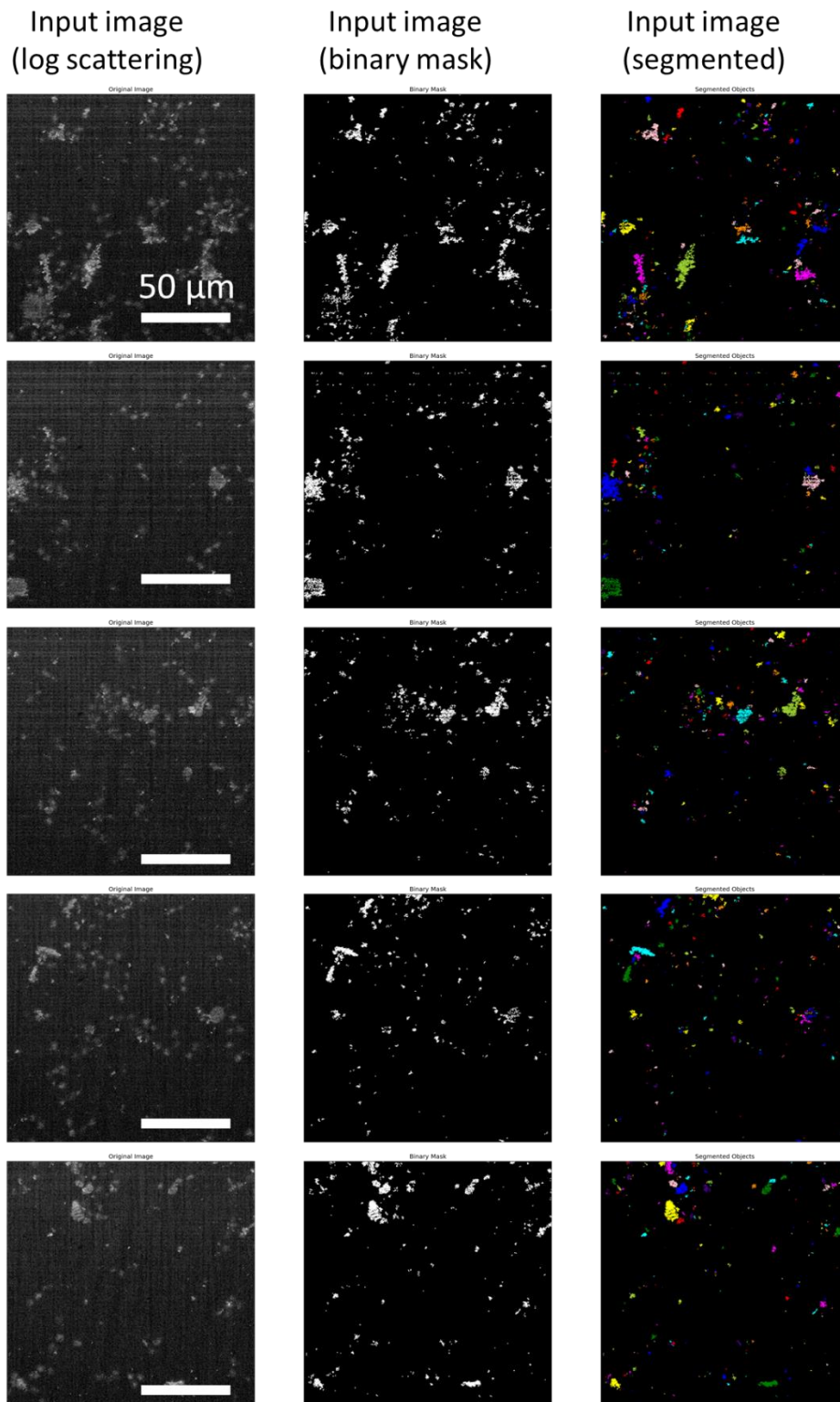


Figure S 16: Log-transformed backscattered signal of 3 μl of Diesel resuspended in the neuronal DMEM/F-12 media. Imaged with the 60X magnification objective after overnight incubation to allow all the material to deposit.

Diesel

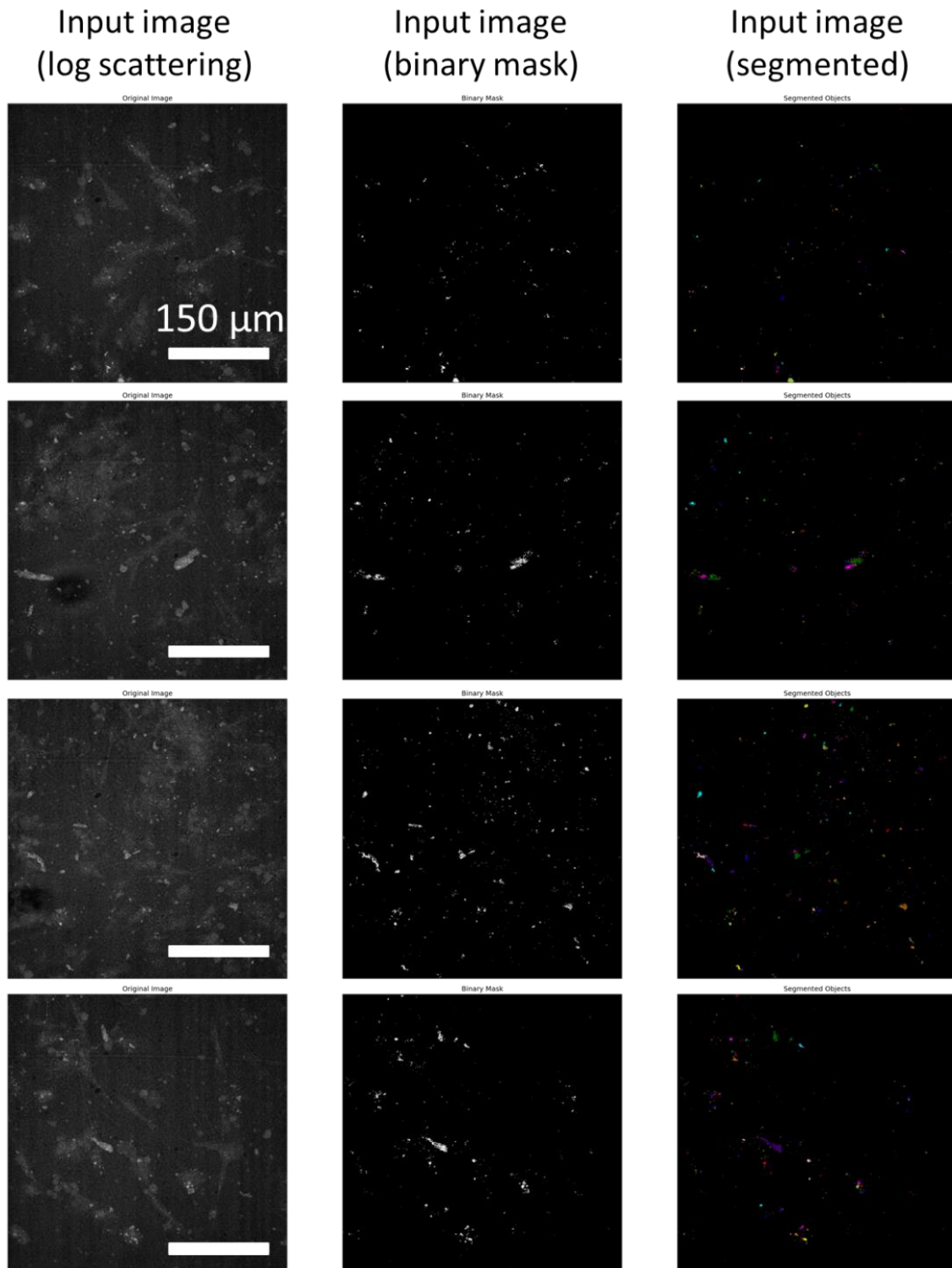


Figure S 17: Log-transformed backscattered signal of 3 μl of Diesel resuspended in the neuronal DMEM/F-12 media. Imaged with the 60X magnification objective after overnight incubation to allow all the material to deposit.

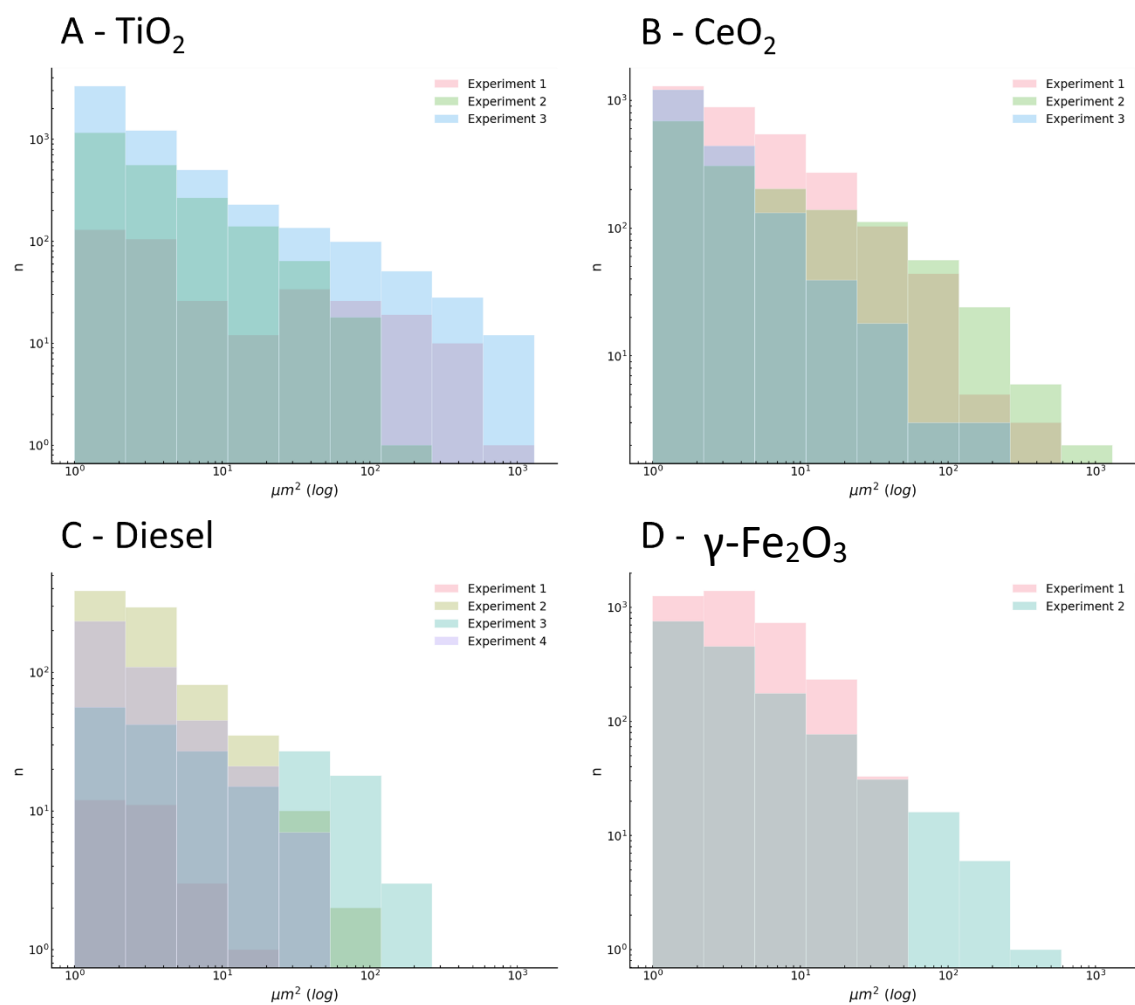


Figure S 18: Log-log distribution of the size of individual particles and aggregates in terms of surface area (μm^2) resuspended in the neuronal cell media for A) TiO₂, b) CeO₂, C) Diesel, and D) maghemite γ -Fe₂O₃.

2 Fluorescent labelling

TiO₂ nanotubes in used in Figure S 22 were labelled with the Alexa 647. In short, the TiO₂ nanotubes were first functionalised with 3-(2-aminoethylamino) propyltrimethoxysilane (AEAPMS) in the dry toluene. The unbound AEAPMS was removed by centrifugation and repeated washing with toluene and hexane. Functionalised TiO₂ nanotubes were then dried and stored in the powder form.

For fluorescent labelling, the functionalised TiO₂ nanotubes were dispersed in 100 X diluted bicarbonate buffer using a tip sonicator. Freshly dissolved Alexa Fluor 647 NHS ester in anhydrous DMSO was added to the dispersed nanotubes and the mixture was sonicated further. The unbound dye was later removed by multiple centrifugal filtrations: first with a mixture of ethanol and diluted bicarbonate buffer, and later with diluted bicarbonate buffer. The labelled TiO₂ nanotubes were stored in diluted bicarbonate buffer at 4 C and used within two weeks after labeling.

The labelling protocol is described in detail by Kokot et al.

<https://doi.org/10.1080/17435390.2021.1973607>

3 Microscope setup

Following incubation with nanomaterial, the living samples were labelled and imaged using a state-of-the-art imaging system consisting of a Microscope Stage Top Chamber (Okolab H301-MIN) incubator mounted on the Olympus (Olympus IX83) confocal fluorescent microscope, which was equipped with the STED laser (Stedycon, Abberior). Stage top incubator maintains atmosphere with the 37°C, 5% CO₂, and >95% humidity to enable long term imaging of living cells.

The images were captured using a confocal microscope equipped with either a 20x magnification objective and 0.8 numerical aperture (NA) lens or a 60x magnification objective with a 1.2 NA lens. The microscope system incorporates four pulsed laser sources (Abberior) with a pulse duration of 120 ps and a maximum power of 50 μW at the sample plane. Additionally, four avalanche photodiode (APD) detectors are utilized for signal detection. Table provides the most frequently used combinations of lasers and filters employed during the experiments. The pulse repetition frequency was 80 MHz. The STED depletion laser, operating at a wavelength of 775 nm, had the same repetition frequency as the excitation lasers, a pulse duration of 1.2 ns, and a maximum power of 170 mW at the sample plane. In cases where the microscope settings were adjusted for maximal resolution during specific experiments, these customized settings will be described alongside the corresponding recorded images later in Supporting Information.

Table S 1. Stedycon lasers and detection filters.

<i>Laser</i> $\lambda_{\text{EXCITATION}}$ (nm)	<i>Laser</i> $\lambda_{\text{EMMISION}}$ (nm)
402	485-495
488	505-550
561	575-625
488	650-700

We successfully detected nanoparticles in the label-free, backscatter detection mode, utilizing the 488 / 488 ± 5 nm excitation / detection combo. Due to the large coherence of the laser, the backscattered light exhibited a strong speckle pattern, which was removed by Fourier transform bandpass filter (1 – 100 pixels) on scattering images. These images were subsequently binarized to obtain nanomaterial masks.

3.1 Main article FIGURE 1 supplementary material

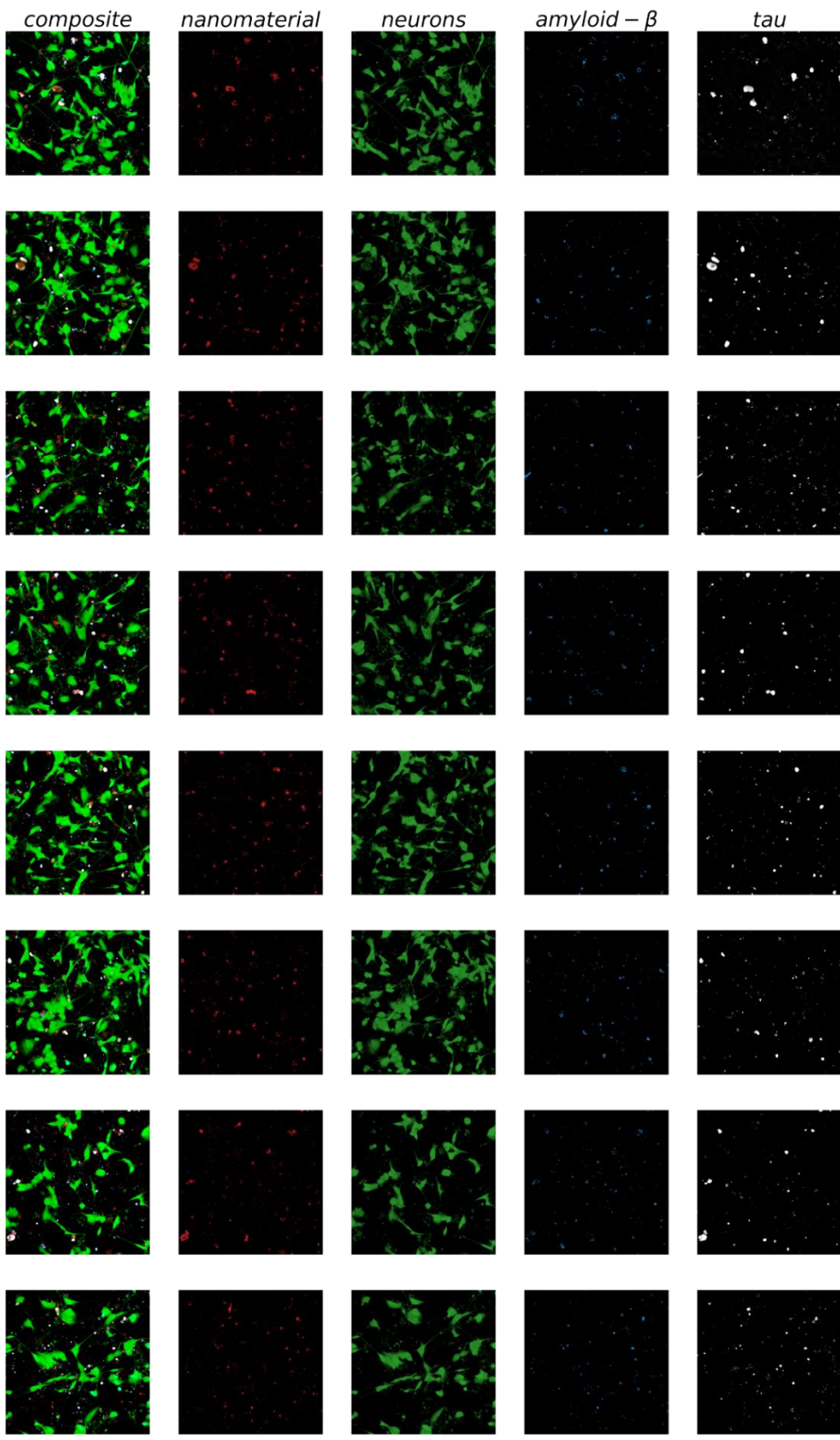
SH-SY5Y cells were subjected to a differentiation process for seven days in DMEM/F12 cell media supplemented with 1% FBS and 10 μM retinoic acid (RA). The media containing RA was refreshed every other day to ensure optimal differentiation. Following the seven-day differentiation period, samples displaying noticeable changes in morphology and significant neurite outgrowth were carefully selected for further experimentation.

To visualize the live cell culture (green), a cytosolic fluorophore called CellTracker™ Green was employed. This fluorophore emits fluorescence exclusively within the cells. Additionally, a mouse monoclonal antibody targeting amino acids 1-40 of human amyloid β ($\text{A}\beta$) was used to detect amyloid precursor protein and $\text{A}\beta$ (blue). Furthermore, a white fluorescence signal was obtained using the Tau-5 mouse monoclonal antibody, which specifically targets total tau. Both antibodies were added in 2 $\mu\text{g mL}^{-1}$ concentration before imaging.

Imaging was performed using a 20x magnification objective with a 0.8 numeric aperture lens, pixel size 250 nm, and the pixel dwell time 10 μs . Specific combinations of lasers and emission filters utilized during the imaging process are provided in Table S Table S2. A total of 15 regions of interest (ROIs), each measuring 400 x 400 μm , were scanned, resulting in the analysis of over 1000 neurons and more than 6000 plaques.

Table S 3. Experimental setup and labels used for the analysis of extracellular plaque content in Figure 1.

<i>Label</i>	$\lambda_{\text{EXCITATION}} \text{ (nm)}$	<i>Laser power (%)</i>	$\lambda_{\text{EMMISSION}} \text{ (nm)}$
CellTracker Green	488	1	505-550
anti- β -Amyloid Ab	488	10	650-700
Backscattering	488	0.3	488



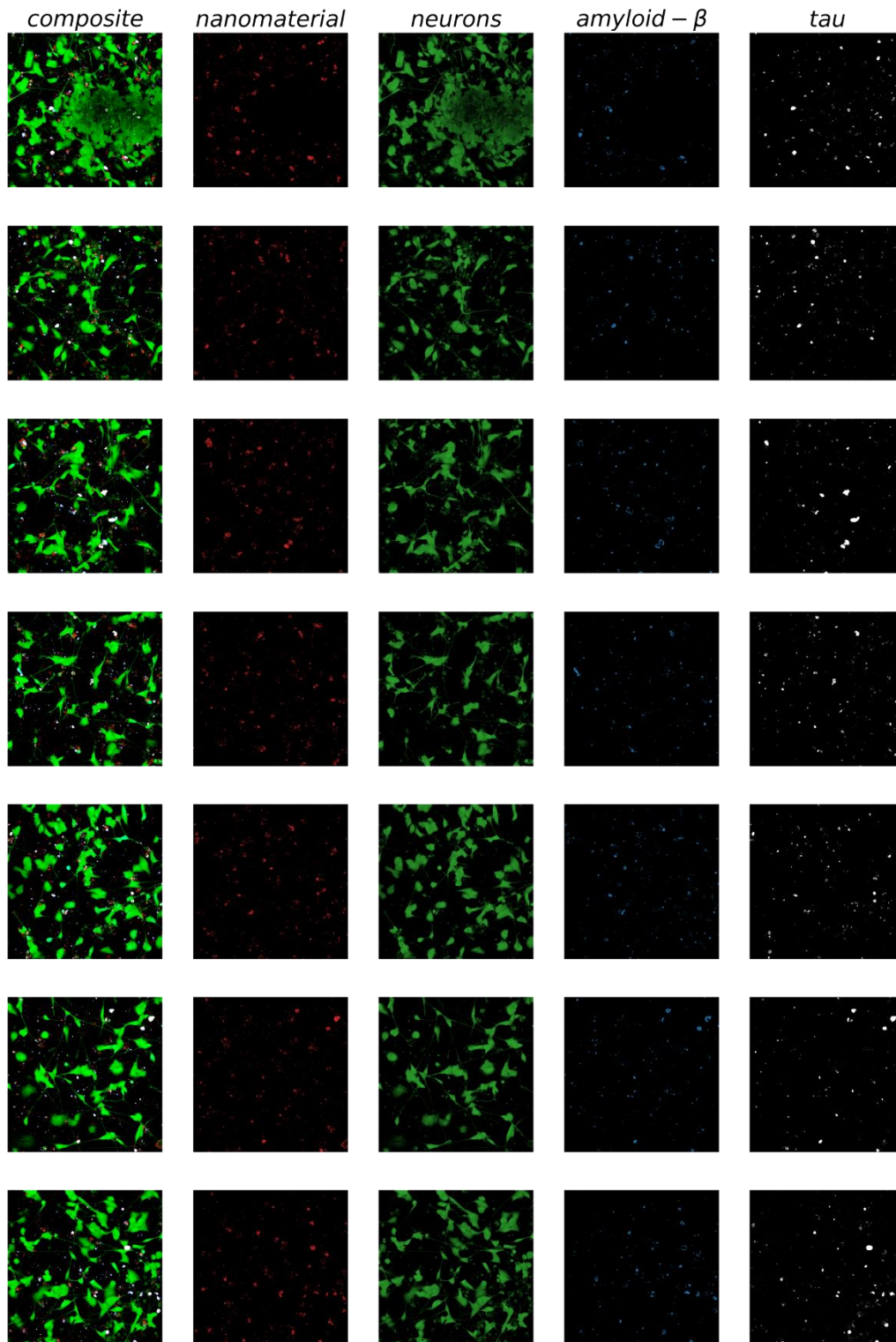


Figure S 19: 15 ROIs analysed for the composition of TiO₂ triggered A β plaques in Figure 1F-G. The first column shows the RGB image, while the subsequent columns display decomposed channels representing different components. Specifically, the second column represents the nanomaterial scattering signal (red), the third column represents the cytoplasmic CellTracker Green label (green), the fourth column represents the anti-A β antibody signal (blue), and the fifth column represents the anti-TAU antibody signal (gray).

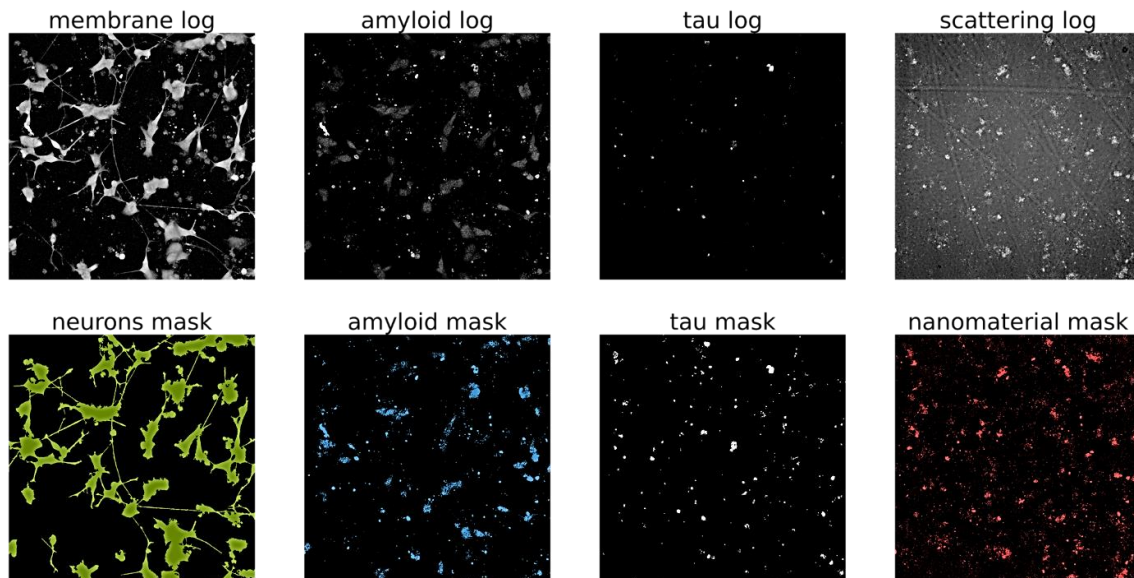
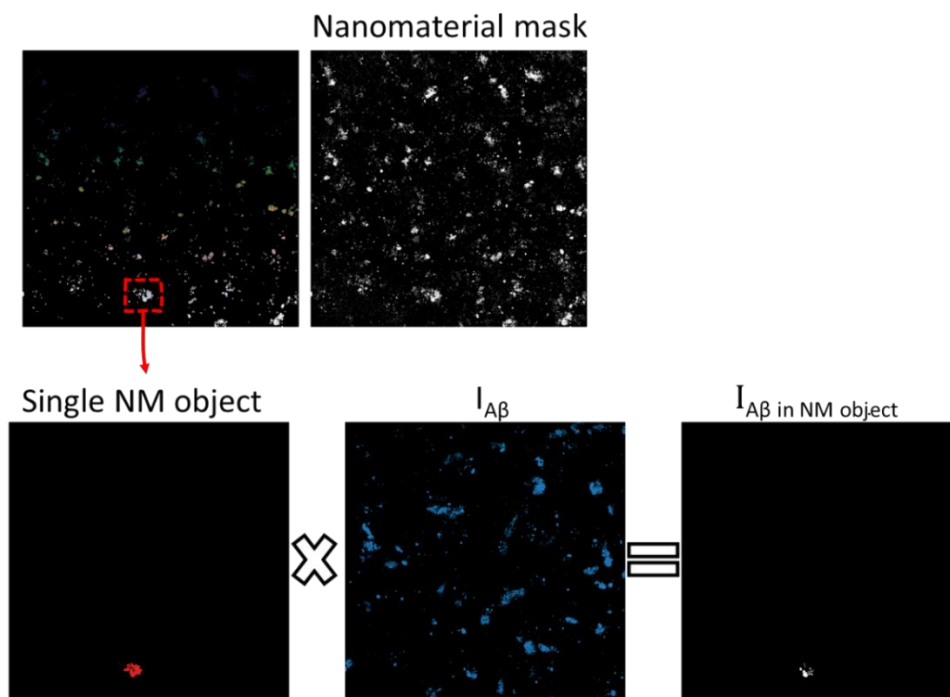


Figure S 20: An example of how image binarization was performed on a single ROI. First, a Fast Fourier Transform (FFT) was applied to all log-transformed images. For the neuron mask, frequencies 2-1500 were kept. For A β , frequencies 1-50 were kept. For tau, frequencies 1-50 were kept. For the nanomaterial, frequencies 1-100 were kept. Afterward, reverse FFT images were thresholded to remove any remaining noise.



$$d_{A\beta} = \frac{\sum I_{A\beta \text{ in NM object}}}{S_{\text{NM object}}}$$

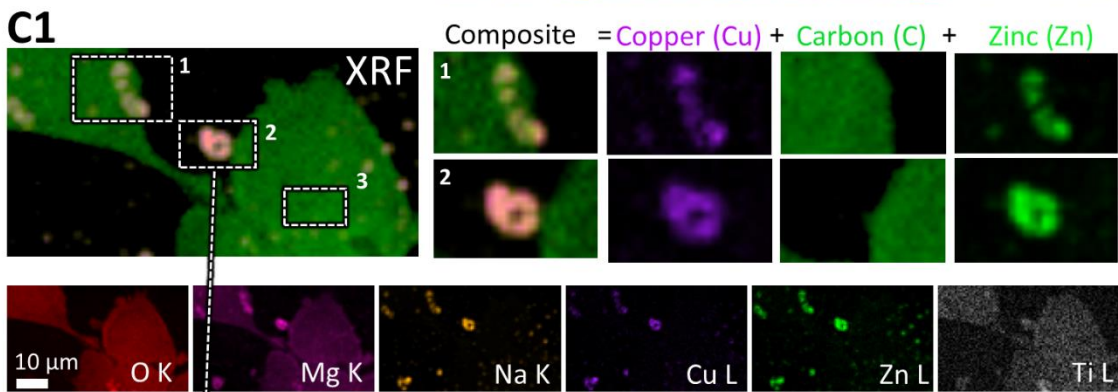
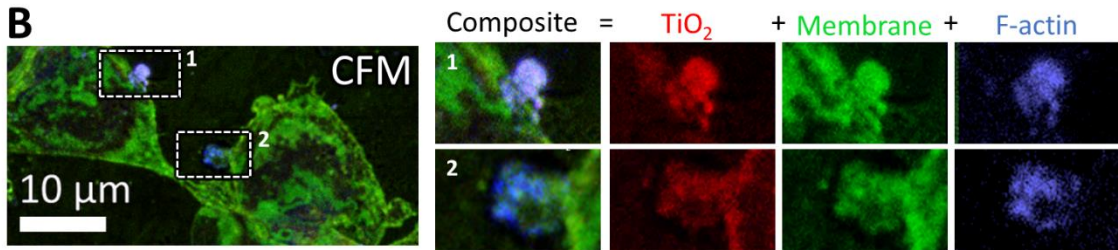
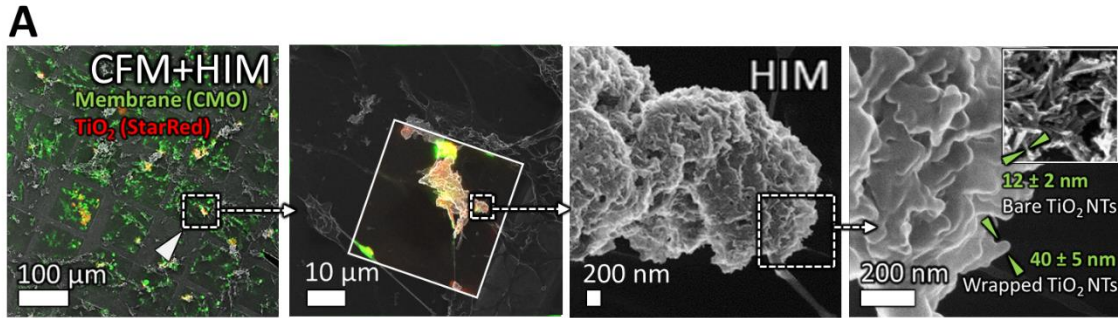
Figure S 21: Example algorithm for calculating densities of plaque components. This algorithm focuses on the calculation of A β density. The process begins with the generation of a binary mask of the nanomaterial using the FFT method, as explained before. Once the mask is obtained, unique IDs are assigned to each nanomaterial object, allowing for individual analysis. Next, a loop is conducted, processing each object individually. The nanomaterial object is multiplied with the input A β micrograph ($I_{A\beta}$), resulting in an image displaying A β fluorescence exclusively within that specific nanomaterial object ($I_{A\beta}$ in NM object). The quotient of the sum of A β intensity within the object and the object's surface area provides the density of A β within that object ($d_{A\beta}$). The same algorithm is applied to the cytoplasmic and TAU signals.

4 TiO₂ nanotubes are present in the extracellular plaques, together with metal ions

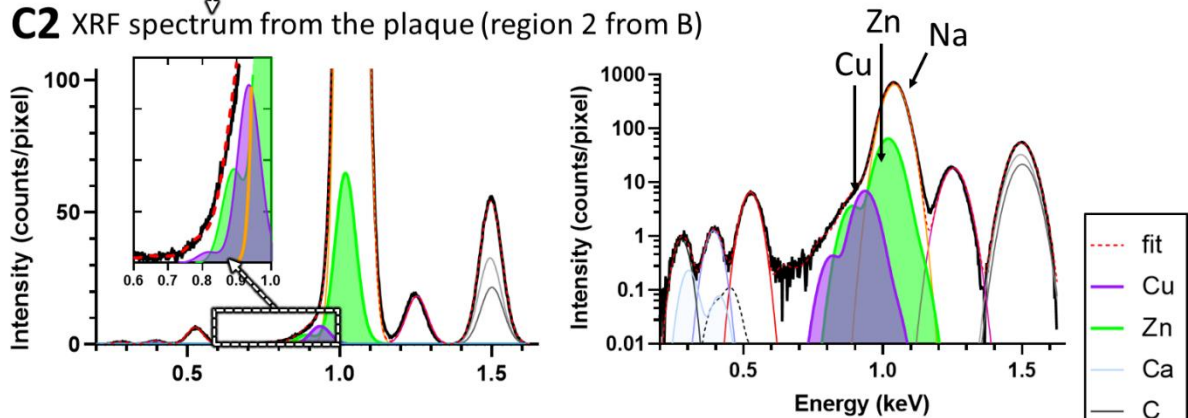
To confirm that the backscattered signal from the extracellular plaques (Figure 1 A-D, red) originates from the TiO₂ nanotubes, we labeled the nanotubes fluorescently (Figure S 22 A, red, TiO₂ (StarRed))¹ to detect and distinguish them from neuronal plasma membranes (Figure S 22 A, green, Membrane) using confocal fluorescence microscopy (CFM). We examined the morphology of the plaques at a higher resolution that can be achieved by optical microscopy using helium ion microscopy (HIM, Figure S 22 A). This approach reveals nanotubes covered with organic material inside the plaques with similar dimensions to bare nanotubes. Bare nanotubes have diameters of around 12 nanometers², whereas the nanotube-like structures within a plaque have diameters of around 40 nanometers (Figure S 22 A inset in the rightmost frame) confirming that the nanotubes are covered with A β and tau.

We next checked whether our *in vitro* plaques resemble the pathological ones also in detailed chemical composition. Metal ions, such as copper, zinc, and iron, impact neurodegeneration by affecting protein structure and misfolding^{3,4}. In AD patients, sub-micrometer copper deposits have been identified in A β plaque cores that are believed to be stabilized within them⁵. Additionally, nickel ions have been shown to interact with A β peptides, promoting the formation of β -sheet structure in A β monomers and directing A β oligomers towards larger, more heterogeneous structures⁶. Native mass spectrometry has revealed that A β peptides strongly bind copper, cobalt, nickel, and iron, and weakly bind magnesium, calcium, manganese, sodium, and potassium⁷.

To determine the elemental composition of the TiO₂ nanotube-induced extracellular plaques, we employed micro X-ray fluorescence (XRF) technique⁸. Comparing the plaques with the cell environment (Figure S 22 C2 versus C3), we identified the presence of increased amounts of copper (purple) and zinc (green), and up to ten times larger amounts of sodium (light orange) in the plaques compared to the cell environment. The elemental maps (Figure S 22 C1) also show that these elements are enriched within the plaques. On fluorescent images, the plaques contain the signal of the nanoparticles (red), plasma membrane probe (green), and actin label (blue) as seen in Figure S 22 B, confocal fluorescence microscopy (CFM).



C2 XRF spectrum from the plaque (region 2 from B)



C3 XRF spectrum from the cell (region 3 from B)

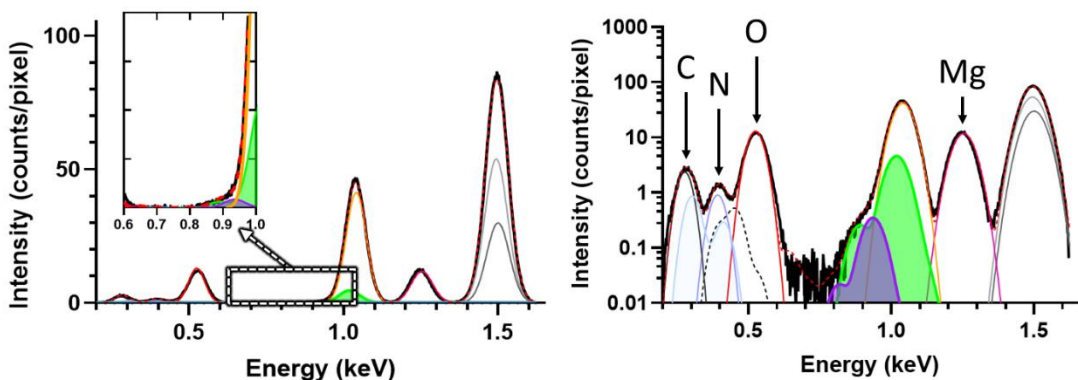


Figure S 22. Extracellular plaques triggered by anatase TiO₂ nanotubes contain the nanotubes, neuronal plasma membrane components, and metal ions. A) Overlay of confocal fluorescence microscopy (CFM) and helium ion microscopy (HIM) images of TiO₂ nanotubes (labeled with StarRed, red) and differentiated SH-SY5Y neuronal-like cells (labeled with CellMask, green) forming plaque-like structures with TiO₂ nanotubes at the core of the plaques (yellow). At high magnification, the nanotubes appear as if they are wrapped with organic material (rightmost frame), differing from bare nanoparticles (inset of the rightmost frame); B) CFM images showing accumulation of the signal of membrane and actin probes at the plaques; C1) Elemental composition of the plaque is presented with X-ray fluorescence (XRF) spectrum from the plaque denoted by frame 2 in B; C2) XRF spectrum from the cell – region denoted by frame 3 in B; Plaques contain up to ten times larger amounts of zinc (light green), copper (blue-magenta), nickel (light yellow), cobalt (light green), iron (light blue), manganese (dark pink), and sodium (light orange); C3) X-ray fluorescence microscopy (μ XRF) images revealing increased concentrations of metals within the plaques, overlapping with elevated concentration of the dyes for F-actin (blue), nanoparticles (red), and neuronal plasma membrane components (green).

4.1 Synchrotron micro-XRF

The XRF data were collected at the TwinMic beamline⁹ of Elettra Sincrotrone Trieste (Trieste, Italy). TwinMic microscope was operated in Scanning Transmission mode where the sample is raster scanned across an incoming perpendicular X-ray beam, delivered by a zone plate diffractive optics. During the scanning a fast ReadOut CDD camera (DV 860, Andor Technology) collects the transmitted X-ray photons, producing absorption and differential phase contrast images¹⁰, while the emitted XRF photons are acquired by 8 Silicon Drift Detector (SDD) located in front of the sample at an angle of 20 degrees in respect to the sample plane¹¹. This results in simultaneous acquisition of sample morphology and elemental distribution.

For our experiment a monochromatic energy of 1.5 keV was chosen to get optimal excitation of Mg, Na, O, Ti and C together with sub-micron spatial resolution. The specimens were scanned at 500 nm step size with a probe size of 600 nm in diameter delivered by an Au zone plate of 600 μ m diameter and 50 nm outermost zone width. An acquisition time of 50 ms pixel⁻¹ and 4 s pixel⁻¹ were used for the CCD and the SDD detector systems respectively.

The acquired XRF spectra were processed by using the PyMCA software package¹². For a better visualization, the raw elemental maps are presented in an animated video (<https://portal.ijs.si/nextcloud/s/ACLp3yGczg6kD85>)

5 Main article FIGURE 3 supplementary material

Neurons were incubated with TiO₂ nanotubes for a duration of 30 hours, followed by labelling and meticulous examination for the presence of TAU and A β -containing plaques. Imaging was conducted using a confocal microscope equipped with a 60x magnification objective and 1.2 NA lens.

For the time-lapse acquisition in Figure 3C, the pinhole was set at 40 μ m (1.6 AU at 650 nm), with a pixel dwell time of 3.3 μ s and a pixel size of 300 nm. The nanomaterial used were the same TiO₂ nanotubes used throughout the study, but they were labelled with Alexa 647. TiO₂ labelling was explained in details previously¹³. The frame rate of the experiment was set to 5 seconds. Links to movies from the main articles are Movie 3C1 (<https://portal.ijs.si/nextcloud/s/sX5weEJQGf5oqCc> for Figure 3C1) and Movie 3C2 <https://portal.ijs.si/nextcloud/s/DZrcdcJ3CQMesAo> for Figure 3C2.

Table S 4. Experimental setup for time-lapse in Figure 3C.

Label	$\lambda_{EXCITATION}$ (nm)	Laser power (%)	$\lambda_{EMMISSION}$ (nm)
CellTracker Green	488	10	505-550
Alexa 647	641	0.3	651-691

To increase the resolution and enhance our understanding of the axonal damage observed in time lapse, we employed a 3D super resolution STED microscopy displayed in Figure 3A,B, and D. Experimental setup is layed out in **Error! Reference source not found.**. The pixel size was 60 nm, pinhole 40 μ m (1.01 AU @650 nm), and pixel dwell time 10 μ s with 1 line accumulation. 3D stacks in Figure 3A and B were acquired with 1 μ m increments for a total of 7 μ m in height.

Table S 5. Experimental setup for STED images in Figure3D.

Label	$\lambda_{EXCITATION}$ (nm)	Laser power (%)	$\lambda_{EMMISSION}$ (nm)	STED power (%)
CellTracker Green	488	1	505-550	50
anti- β -Amyloid Ab	488	10	650-700	74
anti-TAU Ab	640	10	650-700	74
Backscattering	488	0.3	488	/

6 Main article FIGURE 4 supplementary material

The samples were exposed to TiO₂, γ -Fe₂O₃, CeO₂, and diesel exhaust nanoparticles and incubated for 100 hours prior to microscopy. Images were acquired with the 20x magnification objective and 0.8 numeric aperture lens. The excitation/emmission combinations of lasers and detectors used are laid out in

Before differentiation, we seeded approximately 1×10^6 of neurons. Considering that the average mass of a human cell is 3-4 ng (DOI: 10.1039/b615235j), we estimate that we had around 3 mg of cells before exposure to nanomaterials.

Volume of nanomaterials added to cells was 20 μl for all samples. Final mass of the material added to cells and the mass-to-mass ratio of nanomaterial to cell is given in Table S 6.

Table S 6. Mass concentration of nanomaterials used for differentiated neurons exposure.

Material	Mass of added material (mg)	$\frac{m_{NM}}{m_{CELLS}}$ (mg/g)
TiO ₂ nanotubes	0.013	4
γ -Fe ₂ O ₃	0.036	12
CeO ₂	0.032	11
Diesel (DEP9.7)	0.013	3

Table S 7. Experimental setup for images in Figure 4.

Label	$\lambda_{EXCITATION}$ (nm)	Laser power (%)	$\lambda_{EMMISSION}$ (nm)
CMDR	640	1	650-700
anti- β -Amyloid Ab	488	10	650-700
Backscattering	488	1.3	488

Pixel size was 400 nm, pinhole 20 μm (1.01 AU @650 nm), and pixel dwell time 4 μs with 1 line accumulation. 3D stacks were acquired with 4 μm increments for a total of 20 μm in height. Images presented in Figure4A-E are maximum intensity projections.

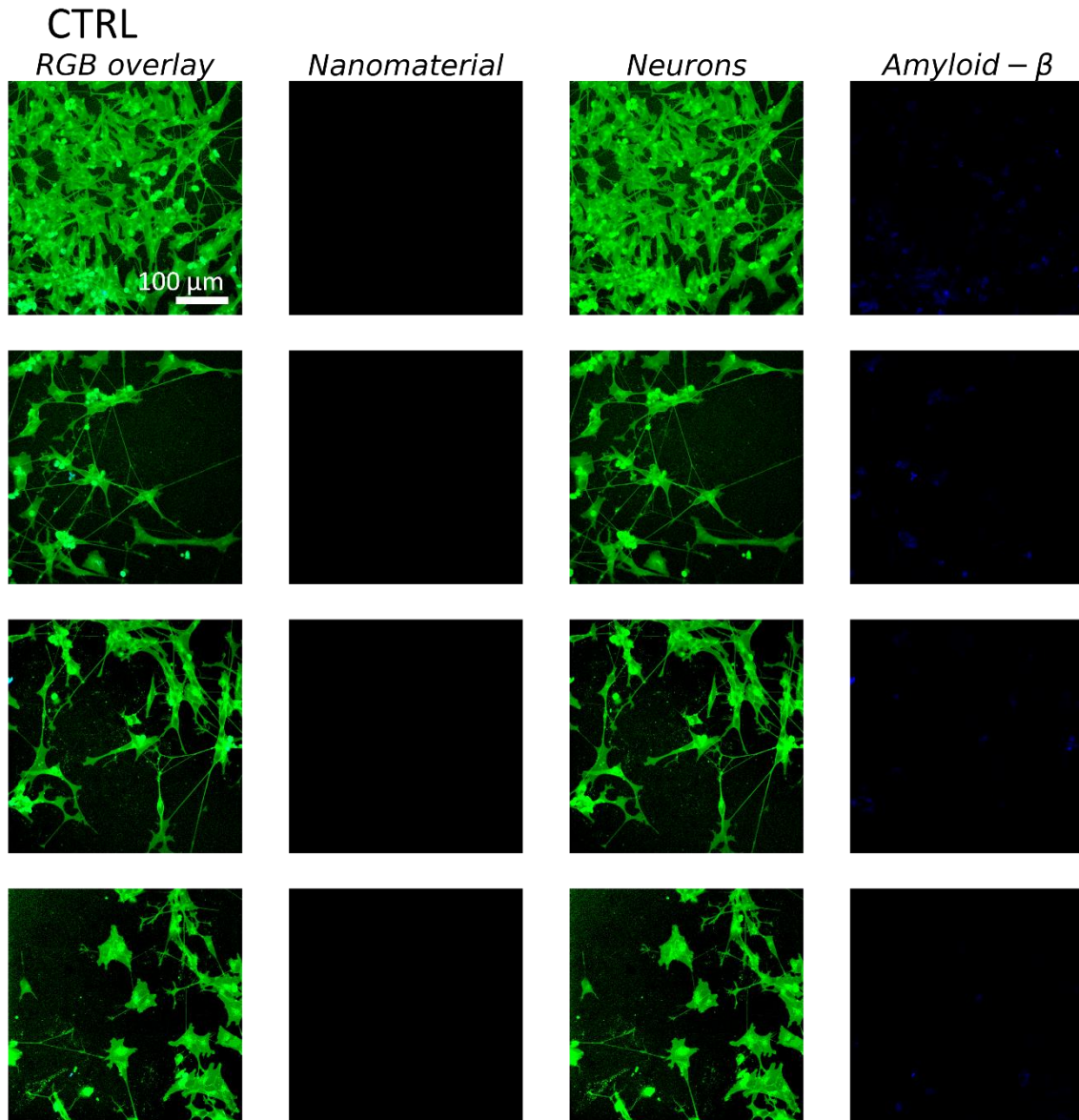


Figure S 23: Micrographs of unexposed control neurons for neurite length measurement. RGB images with plasma membrane label in green (CellMask Orange - CMO) and anti-A β antibody in blue are in the first column. The remaining columns display decomposed channels depicting neurons (CMO) and A β signal, respectively.

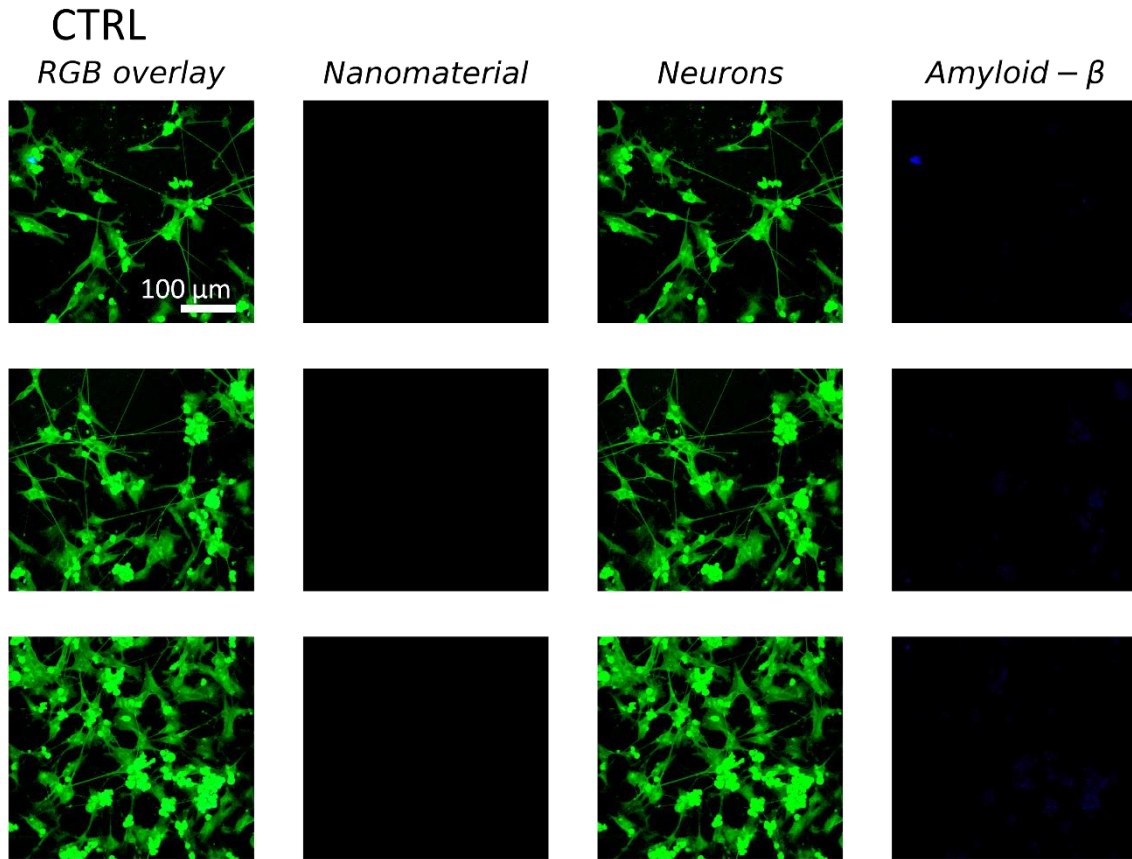


Figure S 24: Micrographs of unexposed control neurons for neurite length measurement. RGB images with plasma membrane label in green (CellMask Orange - CMO) and anti-A β antibody in blue are in the first column. The remaining columns display decomposed channels depicting neurons (CMO) and A β signal, respectively.

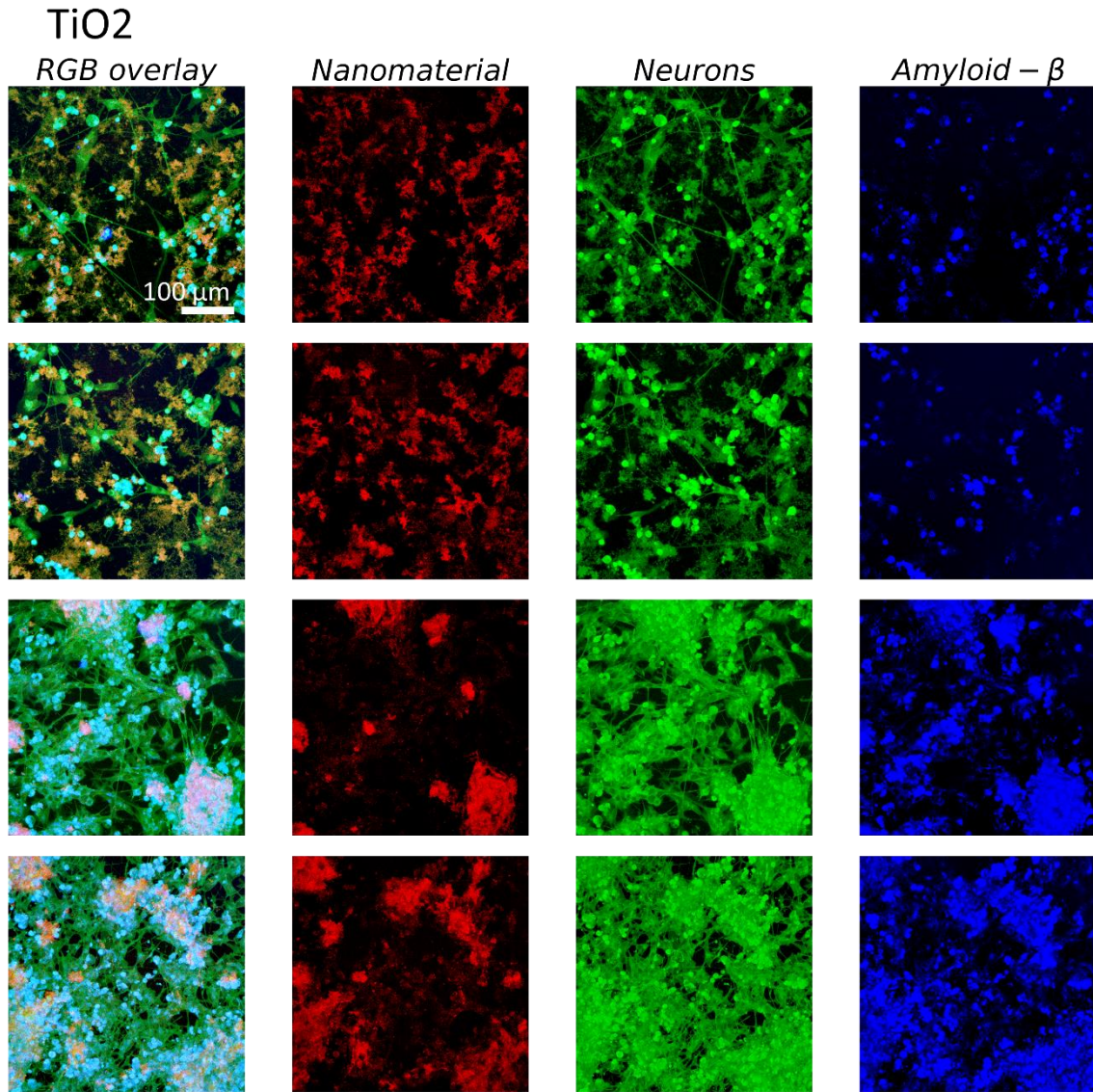


Figure S 25: Micrographs of neurons exposed to TiO₂ nanotubes for neurite length measurement. RGB images with plasma membrane label in green (CellMask Orange - CMO) and anti-A β antibody in blue are in the first column. The remaining columns display decomposed channels depicting neurons (CMO), A β signal, and scattering signal, respectively.

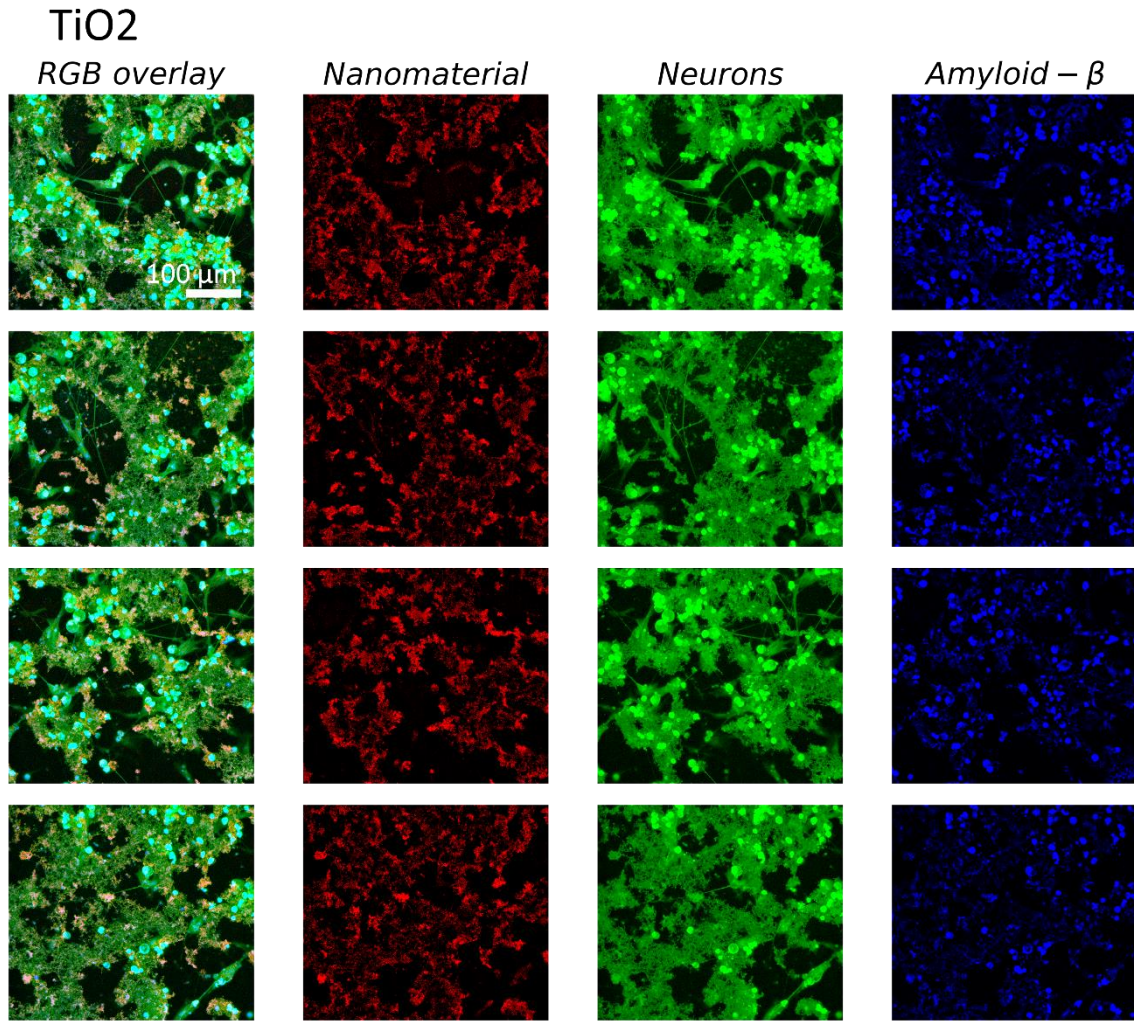


Figure S 26: Micrographs of neurons exposed to TiO₂ nanotubes for neurite length measurement. RGB images with plasma membrane label in green (CellMask Orange - CMO) and anti-A β antibody in blue are in the first column. The remaining columns display decomposed channels depicting neurons (CMO), A β signal, and scattering signal, respectively.

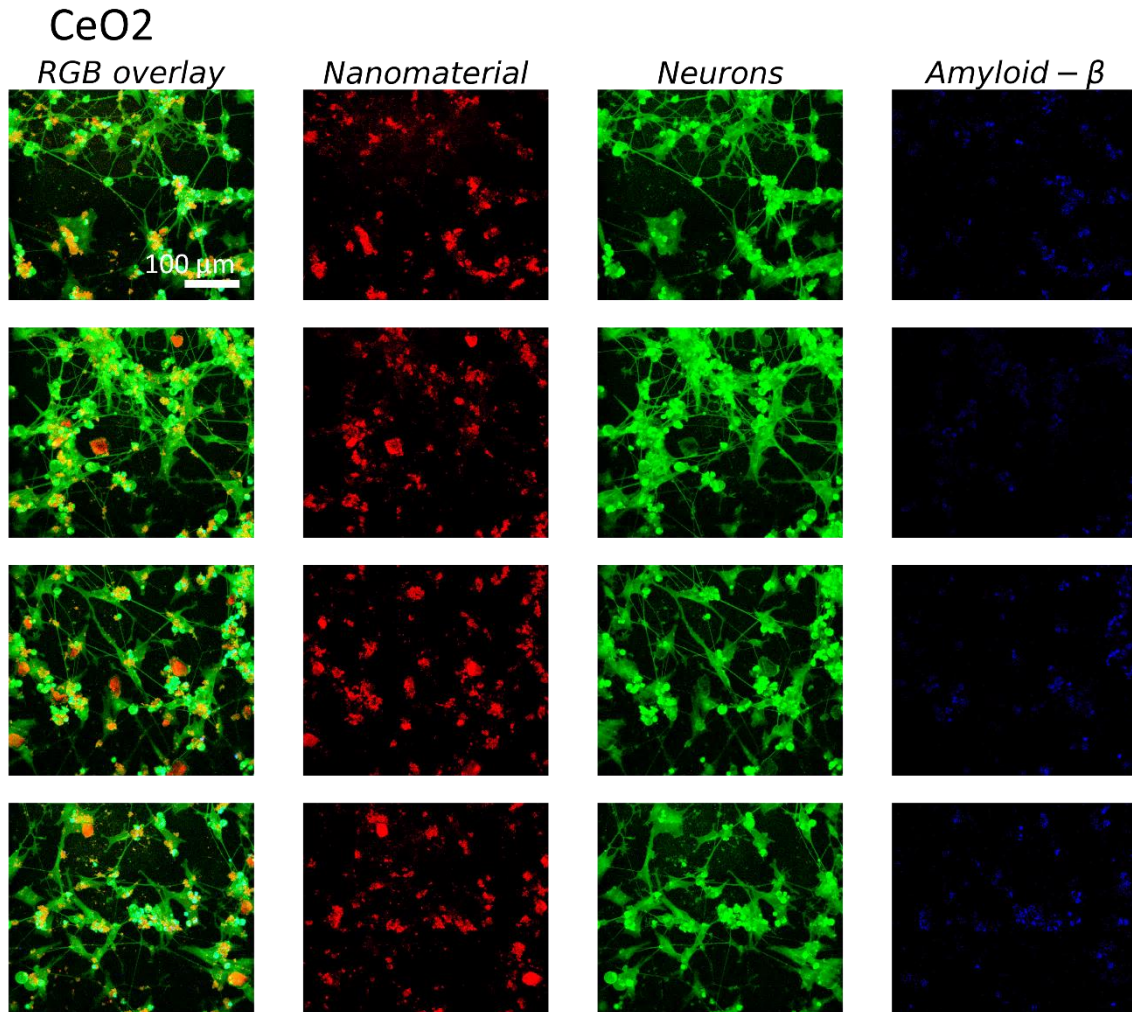


Figure S 27: Micrographs of neurons exposed to CeO₂ for neurite length measurement. RGB images with plasma membrane label in green (CellMask Orange - CMO) and anti-A β antibody in blue are in the first column. The remaining columns display decomposed channels depicting neurons (CMO), A β signal, and scattering signal, respectively.

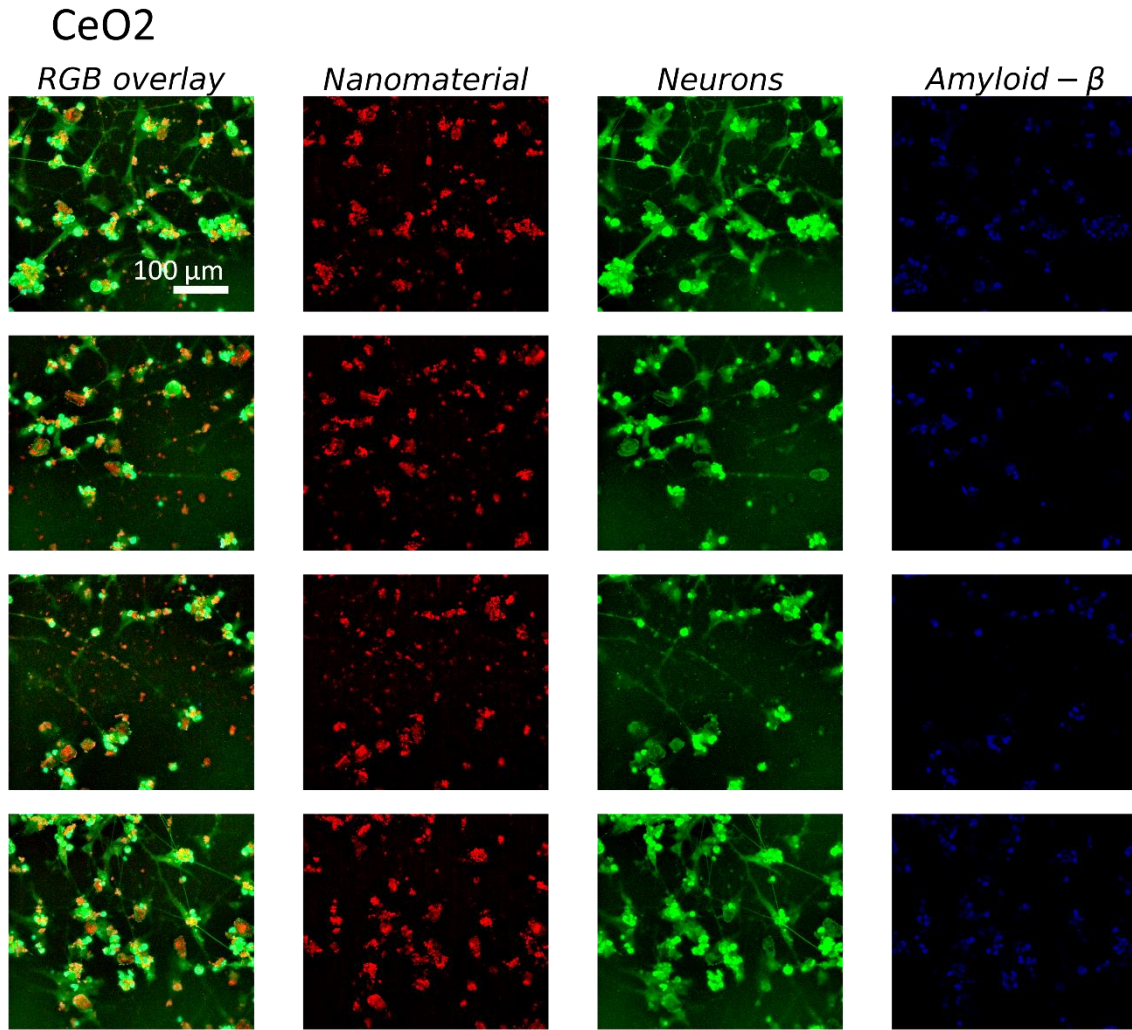


Figure S 28: Micrographs of neurons exposed to CeO₂ for neurite length measurement. RGB images with plasma membrane label in green (CellMask Orange - CMO) and anti-A β antibody in blue are in the first column. The remaining columns display decomposed channels depicting neurons (CMO), A β signal, and scattering signal, respectively.

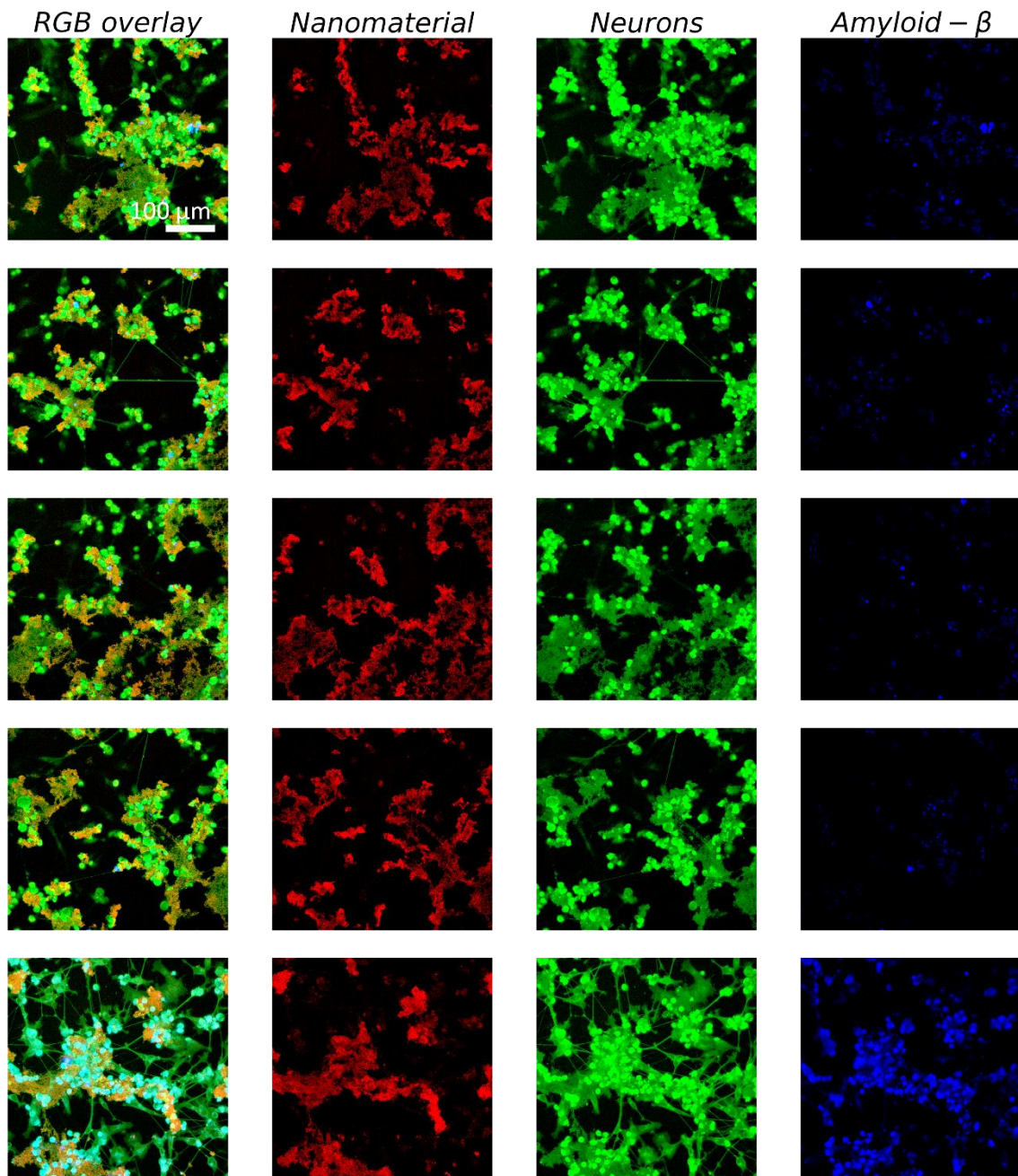


Figure S 29: Micrographs of neurons exposed to $\gamma\text{-Fe}_2\text{O}_3$ for neurite length measurement. RGB images with plasma membrane label in green (CellMask Orange - CMO) and anti-A β antibody in blue are in the first column. The remaining columns display decomposed channels depicting neurons (CMO), A β signal, and scattering signal, respectively.

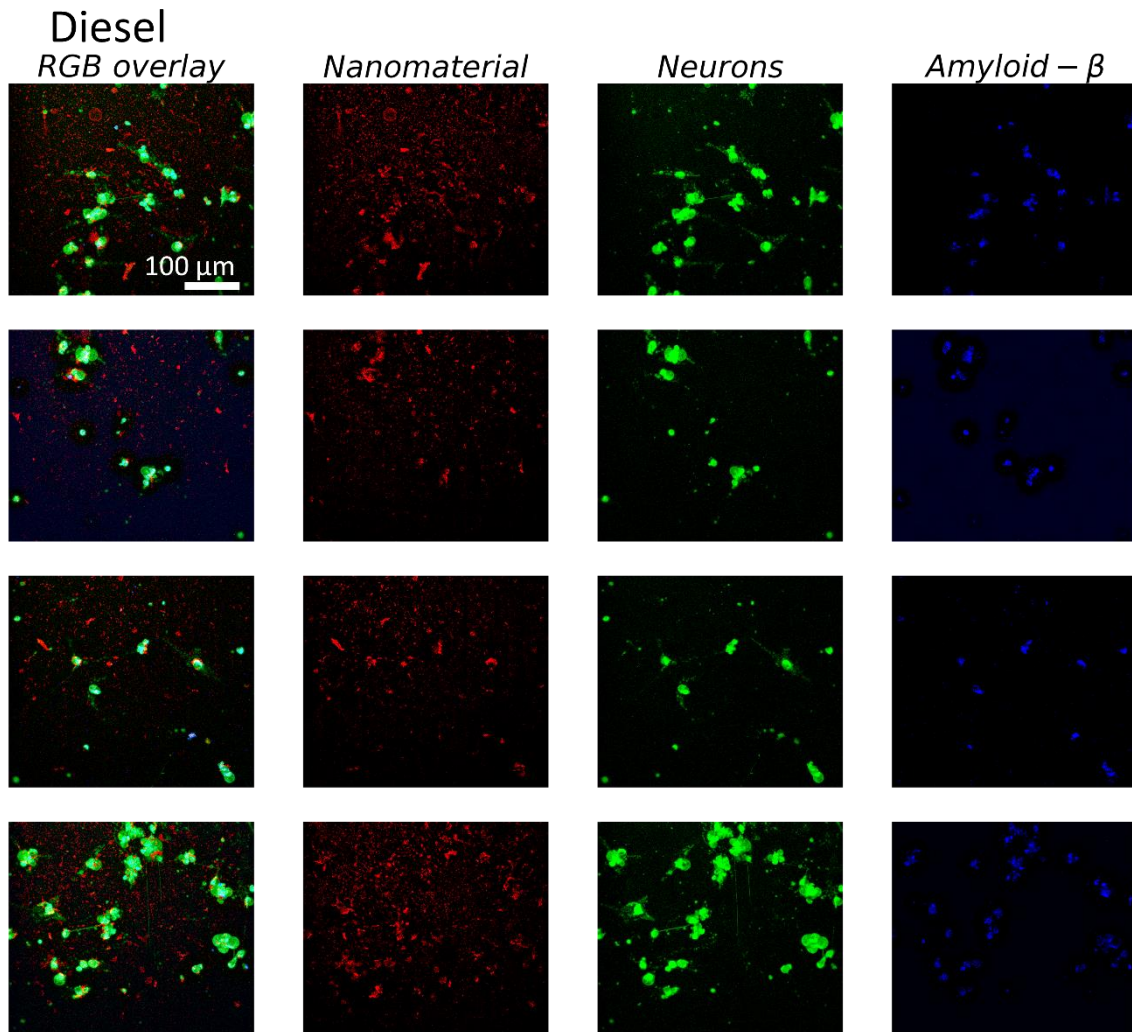


Figure S 30: Micrographs of neurons exposed to Diesel exhaust nanomaterials for neurite length measurement. RGB images with plasma membrane label in green (CellMask Orange - CMO) and anti-A β antibody in blue are in the first column. The remaining columns display decomposed channels depicting neurons (CMO), A β signal, and scattering signal, respectively.

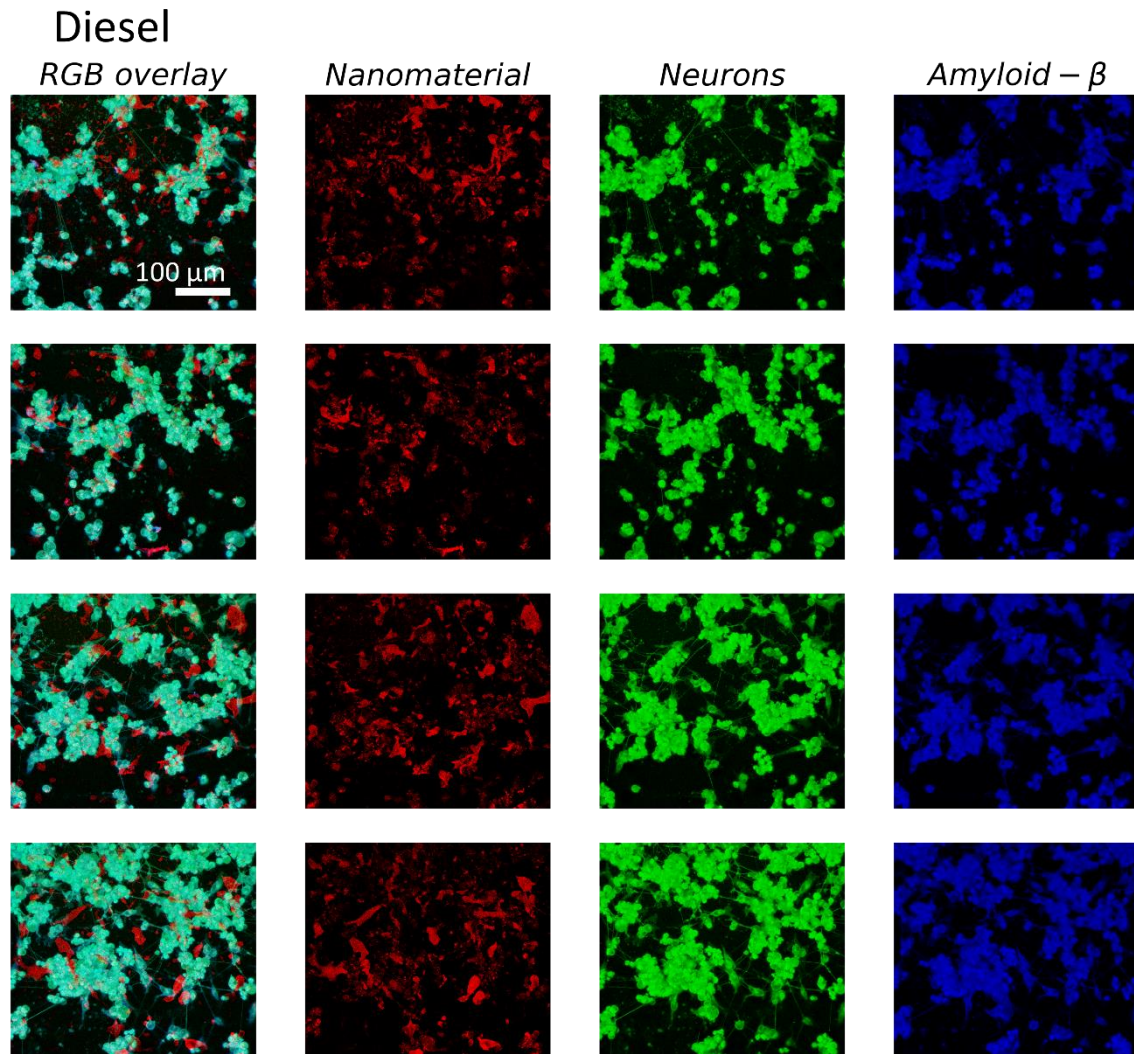


Figure S 31: Micrographs of neurons exposed to Diesel exhaust nanomaterials for neurite length measurement. RGB images with plasma membrane label in green (CellMask Orange - CMO) and anti-A β antibody in blue are in the first column. The remaining columns display decomposed channels depicting neurons (CMO), A β signal, and scattering signal, respectively.

Neurite lengths were analysed using the NeuronJ plug-in, which is available at the following link: <https://imagescience.org/meijering/software/neuronj/>. The analysis was performed in Fiji ImageJ. Manual measurements were conducted to determine the lengths of axons, dendrites, and neurites that connected two distinct cells. Images used in the analysis are depicted in **Error! Reference source not found. - Error! Reference source not found.** Neurites that were measured are overlaid with the violet colour, a default output of NeuronJ plug-in. Subsequently, these measurements were used to plot the distributions of neurite lengths of neurons (Figure S19 and S20) Mann–Whitney U test was performed on the neurite lengths of control, TiO₂, CeO₂, γ -Fe₂O₃, and diesel exposed neurons due to the non-normal distribution of data. Significant difference occurred between the neurite lengths of control and γ -Fe₂O₃ and Diesel exhaust nanoparticles exposed neurons and between TiO₂ and Diesel exhaust particles exposed neurons.

CTRL – marked neurites

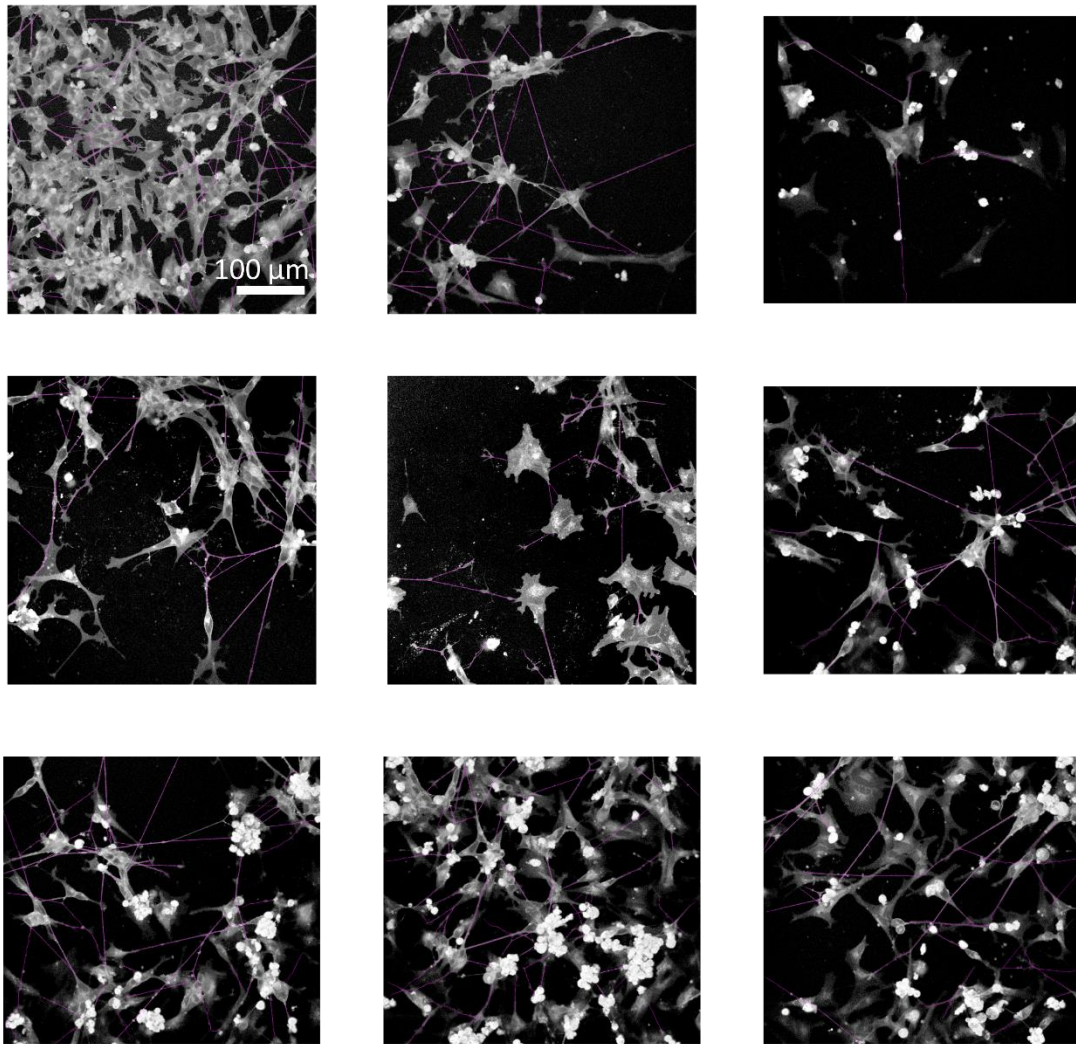


Figure S 32: Images of unexposed control (CTRL) neurons used for the analysis of neurite length (violet).

TiO₂ – marked neurites

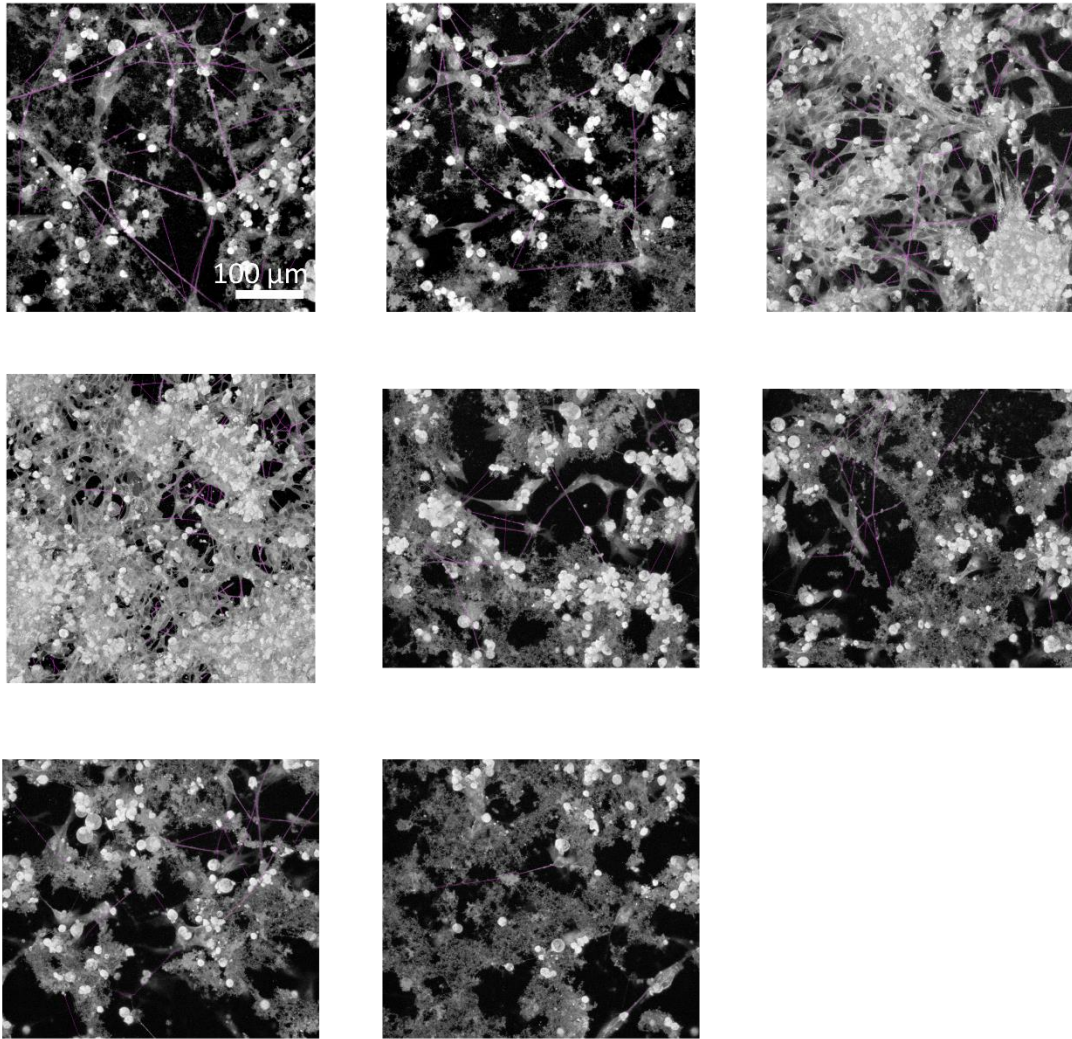


Figure S 33: Images of TiO₂ nanotube exposed neurons used for the analysis of neurite length (violet).

CeO₂ – marked neurites

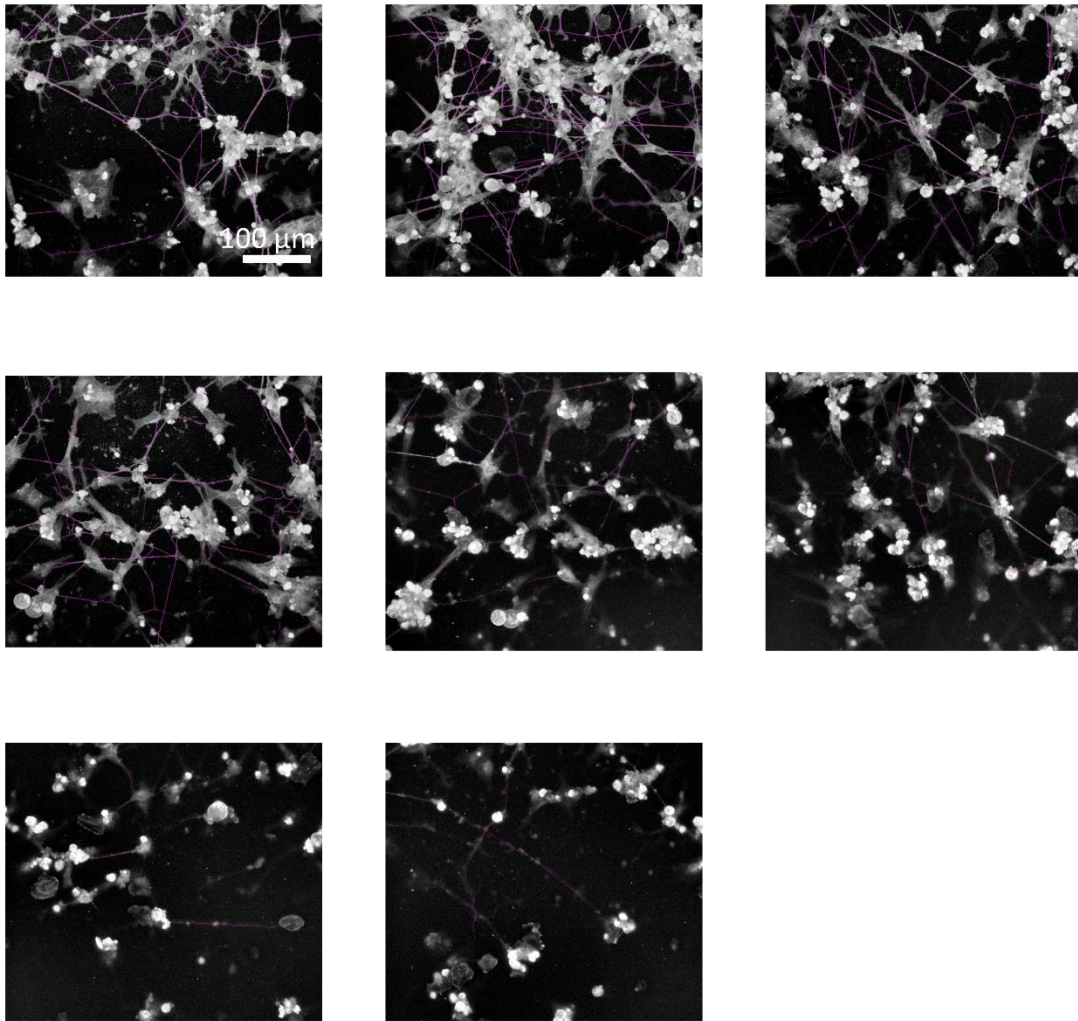


Figure S 34: Images of CeO₂ exposed neurons used for the analysis of neurite length (violet).

Diesel – marked neurites

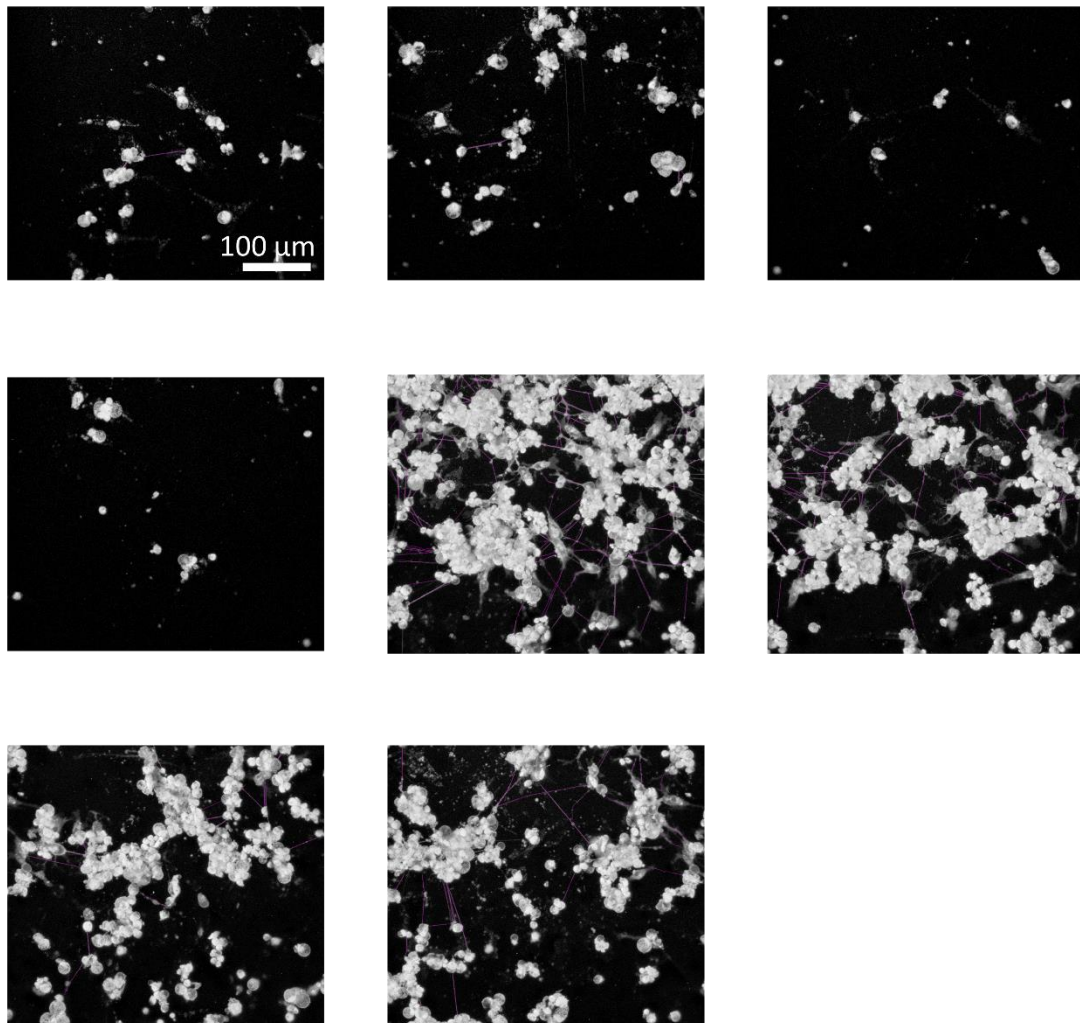


Figure S 35: Images of Diesel exposed neurons used for the analysis of neurite length (violet).

maghemite $\gamma\text{-Fe}_2\text{O}_3$ - marked neurites

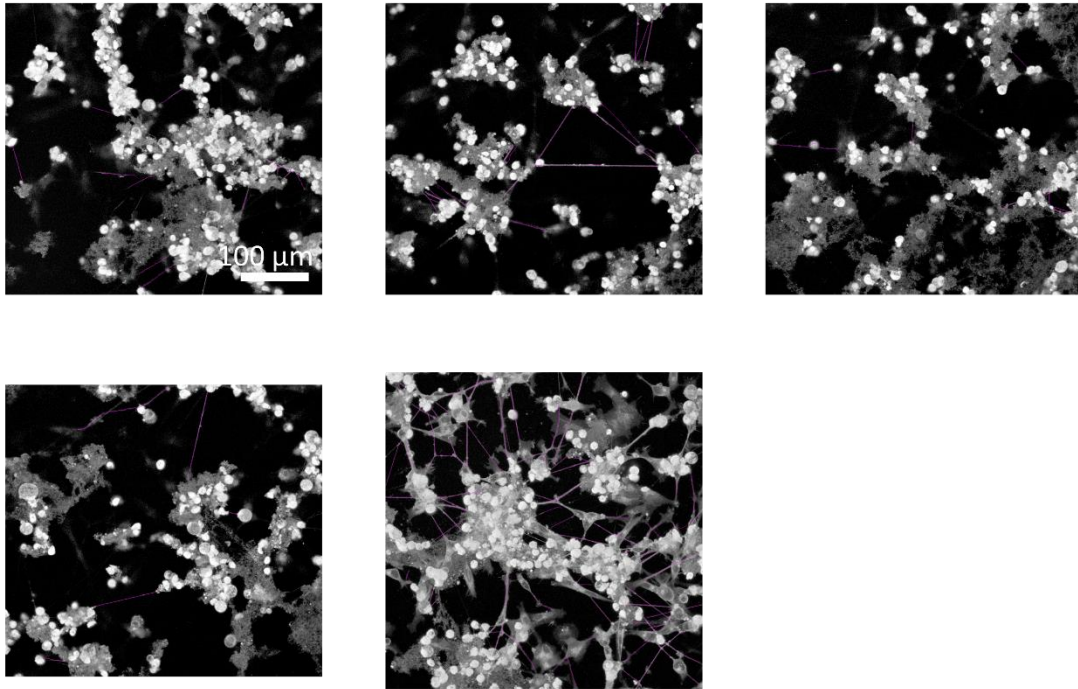


Figure S 36: Images of $\gamma\text{-Fe}_2\text{O}_3$ exposed neurons used for the analysis of neurite length (violet).

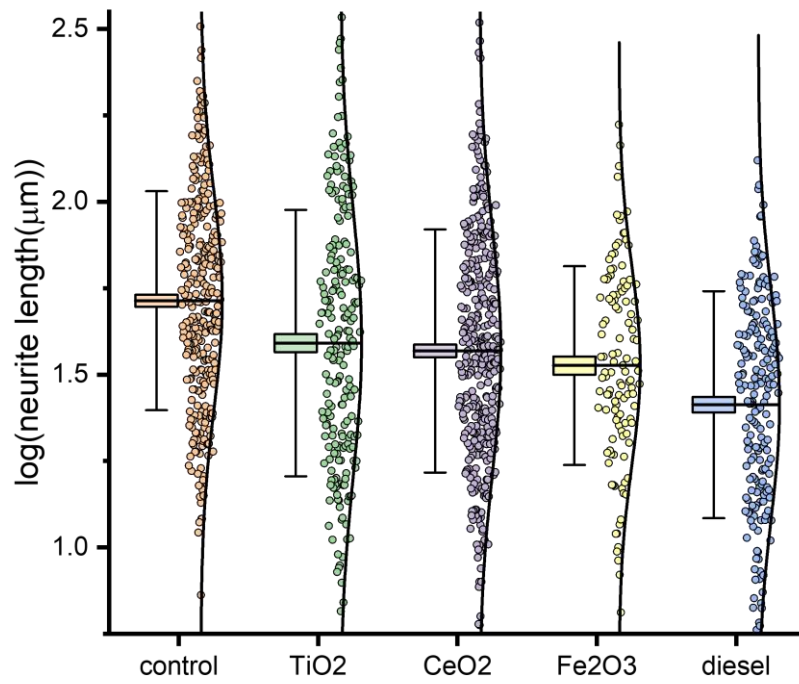


Figure S 37: Distribution of log-transformed neurite lengths of neurons in control, TiO₂ nanotube, CeO₂, γ-Fe₂O₃, and diesel exhaust particles exposed groups.

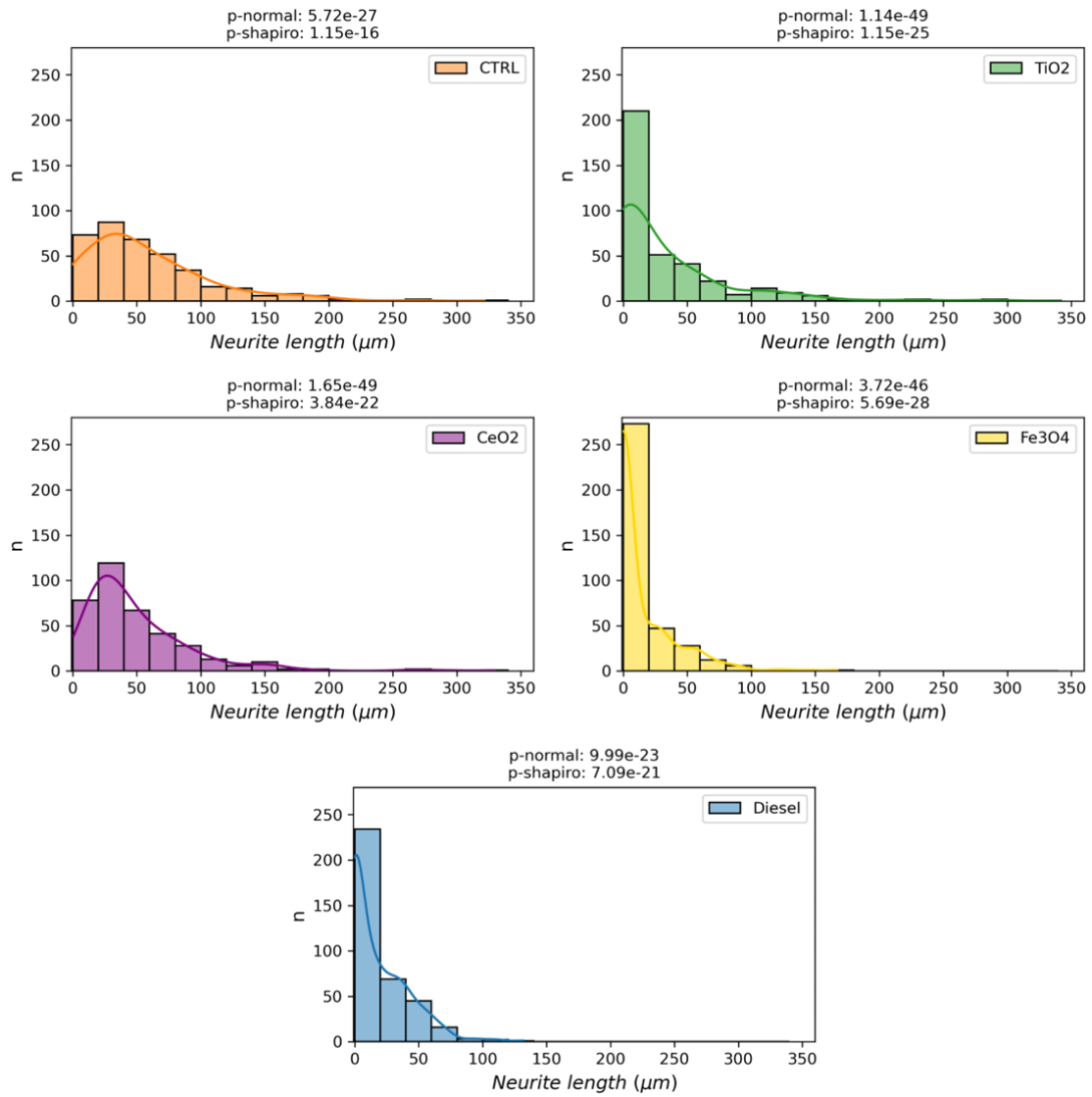


Figure S 38: Histograms of neurite lengths of control, TiO_2 , CeO_2 , Fe_2O_3 , and diesel exhaust particles exposed neurons. Data distribution for all groups is not normal as indicated by the histogram shapes. The normality of the data was further assessed using the D'Agostino and Pearson's Test and Shapiro-Wilk. Test p-values, p -normal and p -shapiro, respectively, < 0.05 indicate a deviation from normality.

For the analysis involving the intensity of A β and the proportion of A β signal colocalized with nanomaterial, Python scripts were utilized. The algorithm outlining the steps of this analysis can be found in **Error! Reference source not found.**

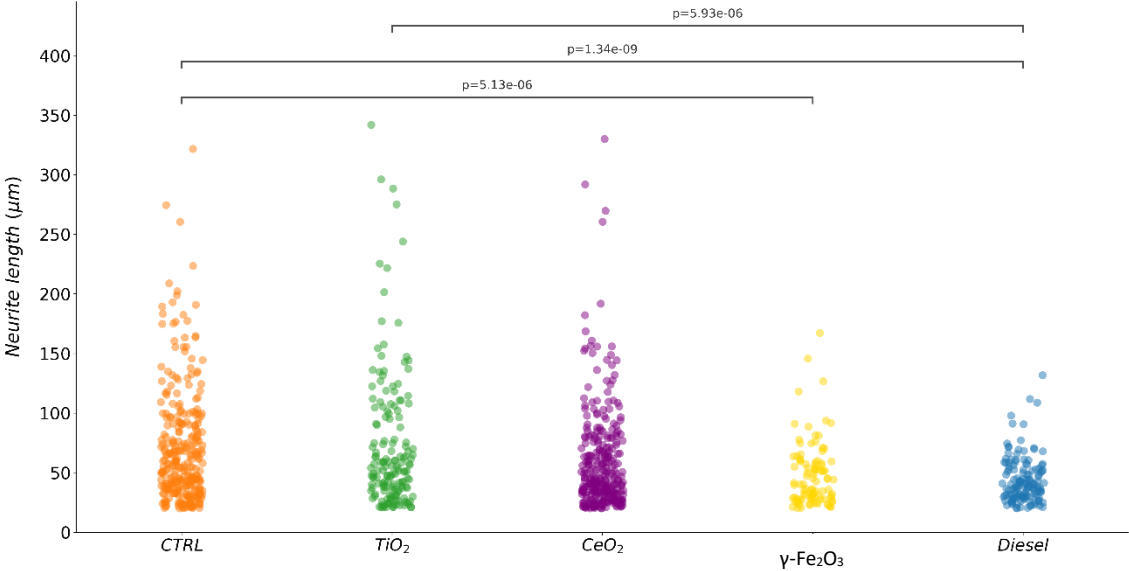


Figure S 39: Mann–Whitney U test was performed on the neurite lengths of control, TiO₂, CeO₂, Fe₂O₃, and diesel exposed neurons due to the non-normal distribution of data. Significant difference occurred between the neurite lengths of control and Fe₂O₃ and Diesel exposed neurons and between TiO₂ and Diesel exhaust particles exposed neurons.

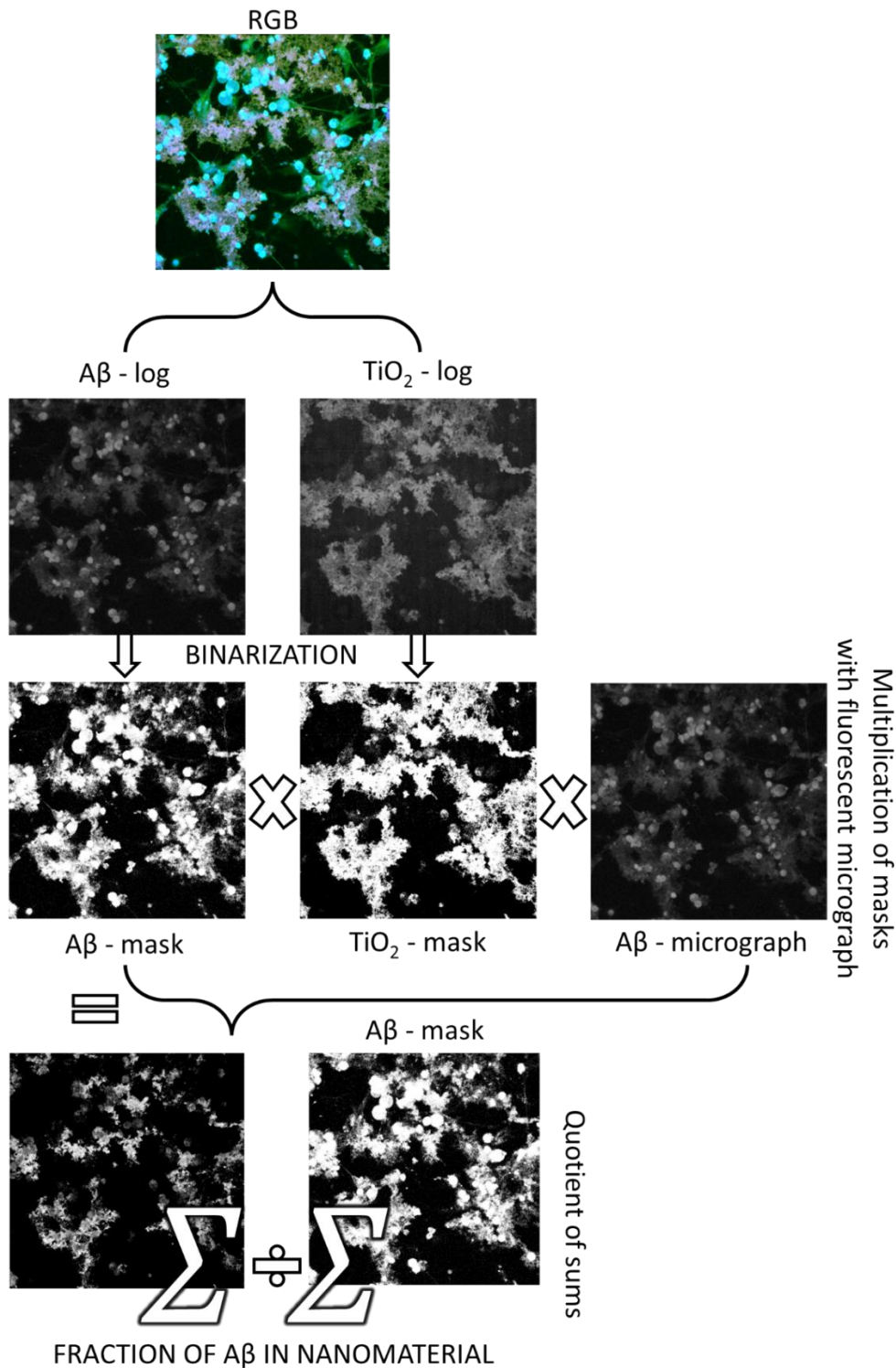


Figure S 40: Aβ and total nanomaterial binary masks for Aβ intensity and Aβ fraction in nanomaterial calculation. Initially, RGB micrographs were decomposed into individual channels, which were then subjected to a logarithmic transformation. A Fast Fourier Transform bandpass filter was applied to eliminate structures smaller than 2 pixels and larger than 800 pixels in diameter for both the nanomaterial and Aβ channels. This effectively remove all objects smaller than 400 nm in one dimension (pixel size = 200 nm). Subsequently, the images were binarized to generate masks. To determine the density of Aβ plotted in Figure 4 of the main paper, we used the same algorithm as explained in Figure S 21. To assess the fraction of Aβ present in nanomaterial aggregates, the Aβ mask was multiplied with the nanomaterial mask, resulting in the co-localization of both masks. The surface area of this product divided by the surface area of the Aβ mask yields the fraction of Aβ in nanomaterials.

7 Dose relevance

In order to determine whether the dosage we administered are relevant for human exposure we estimated the dose that might accumulate in the brain in two ways:

1) we searched the literature for the amount of each nanoparticles found in the brain of Alzheimer's disease patients and found that in the case of diesel exhaust and iron oxide the concentrations we used are not far from the amounts found in the brain.

2) estimated the transport of nanoparticle to the brain considering different routes using the data found in the literature as explained below:

7.1 the amount of nanoparticles found in the brain of Alzheimer's disease patients

TiO₂ nanotubes are an engineered nanomaterial relevant to occupational risk. CeO₂, iron oxide (γ -Fe₂O₃), and diesel exhaust are examples of particulate matter found in polluted air and are relevant as a public health risk. We selected CeO₂ due to its predominantly nontoxic nature, whereas iron oxide and diesel exhaust (DEP9.7) nanoparticles are linked to neurodegenerative diseases by epidemiological studies. Iron oxide nanoparticles were found in the brains of Alzheimer's disease patients living in polluted areas, such as Mexico City.

TiO₂, as a white pigment, is used as a food additive in personal care products (e.g. toothpaste) and in many other consumer products. It contains a fraction of nanosized primary particles (<100 nm)^{14,15}. Titanium can be found in human tissue at lower average concentrations ranging from 1 μ g/g¹⁴ up to 80 μ g/g¹⁶ in the human brain. We used a very high concentration of 3 mg/g, which resulted in extracellular amyloid beta plaque formation, yet the lengths of neurites didn't decrease as much as in the case of diesel exhaust nanoparticles, despite the high concentration used. Several in vivo studies reviewed by Song et al.¹⁷ have demonstrated that the TiO₂ NPs can be transported and accumulated in the brain, but mostly in intranasal instillation or inhalation studies, eventually leading to CNS dysfunctions. Titanium content in mouse hippocampus after 90 days of continuous intranasal exposure to TiO₂ nanoparticles was 0.6 mg/g tissue at the highest administered dose of 10 mg/kg body weight¹⁸, which is also much higher than the levels observed in humans. Thus, neuroinflammation and impairment of spatial memory observed in mice and our in vitro experiment occur at more than 10 times higher brain content than it is found in humans. The effect of TiO₂ nanoparticles on the brain is thus still controversial since detrimental effects are observed at very high doses, which are not observed in human tissues.

On the other hand, we estimated the relevance of our exposure levels also by considering The National Institute for Occupational Safety and Health recommends occupational exposure limits of 2.4 mg/m³ for fine TiO₂ and 0.3 mg/m³ for ultrafine (including engineered nanoscale such as TiO₂ nanotubes we used in this manuscript). Assuming breathing rate of 15L/h, 40-hour week and body mass 70kg, one would have to breath about 3000 years to obtain the dose 3 mg/g body mass, where we neglected that exposed dose might not distribute equally over entire body mass but might accumulate preferentially in the brain during nasal breathing on one hand, and that not all of the nanoparticles are retained in the body on the other hand. Since the TiO₂ nanotubes didn't induce shortening of the neurites event at such high levels used in this manuscript we can conclude that TiO₂ nanotubes probably don't induce neurodegeneration and that the controversy regarding the neurotoxicity of TiO₂ observed in animals might arise from the high levels used in animal studies.

CeO₂ nanoparticles are used as fuel additive in motor vehicles to reduce carbon monoxide, nitrogen oxides, and hydrocarbons in exhaust gases, thus the particles are released in the air.

Effects of CeO₂ nanoparticles are contradictory, demonstrating all kinds of effects, from protective to toxic¹⁹. For example CeO₂ nanospheres and nanorods improved cognitive impairment following mild

traumatic brain injury in VC57BL/6J male mice at the dose of 0.02 mg/g body weight, although the concentration in the brain was not reported ^{19,20}.

The mean magnetite **iron** oxide (Fe₂O₃) concentration of several millimeters large, chemically unfixed post-mortem tissue from Alzheimer's cases can reach up to 400 µg/g ²¹. However, brain iron oxide (magnetite) airborne particles can be highly concentrated in sub-micrometer regions in the human brain ²². Such magnetite nanospheres are ubiquitous and abundant in airborne particulate matter pollution. They are <~200 nm in diameter and can enter the brain directly via the olfactory bulb ²². Examination of the human frontal cortex brain samples obtained from subjects who lived in Mexico City revealed that magnetite nanoparticles have an external, rather than an endogenous source ²². Although the highest brain magnetite concentration was 10 µg/g dry tissue, the transmission electron micrographs of brain thin sections showed that the nanoparticles are located in about 1% of the total area. Considering that some regions don't contain nanoparticles, we can assume that the local concentration of nanoparticles can be up to 100 times higher as compared to larger brain regions. Therefore, we can safely assume that relevant in vitro cell line exposure is about 1 mg/g, which about ten times less (12 mg/g) the levels we used. Thus, we believe that the toxic effect of the iron nanoparticles in the in vitro cell line system we used might not be relevant to human exposure.

We couldn't find the levels of **diesel exhaust** particles in brain tissue since they are mainly composed of carbon and probably can't be differentiated from the tissue. However, iron is present in most of diesel exhaust samples, the iron content can vary from 8 weight % to 55 weight %, being on average about 20 weight % ²³. Thus if we assume that the iron accumulated in samples of Alzheimer's cases which can reach up to 400 µg/g ²¹ originates from diesel exhaust particles then the brain burden of diesel exhaust particles might reach up to 2 mg/g tissue weight. We used 3 mg/g, thus the neurite degeneration and apoptosis of neurons we observed in cell culture might be relevant to diesel exhaust exposure.

7.2 Estimate of the transport of nanoparticle to the brain

7.2.1 Traversal through the blood-brain barrier

The presumed routes of inhaled particle migration comprise traversal through the blood-brain barrier or translocation along the olfactory nerve. Both pathways begin with the inhalation of airborne particles, where after mucus and ciliary protrusions of cells in the upper respiratory region trap the majority of inhaled particles. Only PM_{2.5} and smaller particles, including nanoparticles with at least one dimension under 100 nm, can evade these defence mechanisms, eventually reaching the alveoli of the lower respiratory tract. In the ensuing weeks, majority of these nanoparticles are naturally excreted from the body ²⁴, while a subset remains and become sequestered. Some of these nanoparticles can potentially relocate from the alveoli to the bloodstream ²⁵. However, due to the minute volume of translocated nanoparticles and the large volume of blood, the accumulation of these nanoparticles at the blood-brain barrier in quantities required for pathological changes would take hundreds of years of inhaling air polluted with 40 µg m⁻³ PM_{2.5}, making the first hypothesis less plausible.

7.2.2 Transport along the olfactory nerve

On the contrary, the second pathway, involving nanoparticle translocation along the olfactory nerve, emerges as a more plausible route, because the distance between the brain and nasal mucosa is only a few centimetres. Furthermore, axons of olfactory neurons extend to the nasal mucosa on one end, and synapse with regions intrinsically related to neurodegeneration, including the hippocampus, hypothalamus, and prefrontal cortex ²⁶, on the other end.

7.2.3 Rapid accumulation of nanoparticles in the olfactory bulb:

De Lorenzo had intranasally administered exogenous 50 nm large gold colloidal particles to rats and found them to be present in the neurons of olfactory bulb already in 30 - 60 minutes after exposure²⁷. Similarly, fluorescence and transmission electron microscopy imaging of mice olfactory bulb sections, three hours after inhalation of aerosolized quantum dots, revealed their presence along olfactory nerves. Importantly, this presence coincided with microglia activation, as evidenced by weak RCA-1 staining and amoeboid morphology. This contrasted with RCA-1 positive resting microglia displaying a branched morphology²⁸.

7.2.4 Delayed accumulation of nanoparticles in the deep brain structures:

Oberdörster et al. examined the accumulation of insoluble 39 nm [¹³C] in lungs, olfactory area, cerebrum, and cerebellum of mice following double 6h-long inhalation. While the amount of [¹³C] in the lungs rapidly rose post-exposure, 50% was cleared within seven days. However, in brain tissues, [¹³C] concentration was smaller at 1-day post-exposure but did not decrease at 3-, 5-, or 7-days post-exposure. Notably, the olfactory area showed continuous [¹³C] accumulation, suggesting a continuous delivery and a lack of efficient clearance mechanisms²⁹. In a separate study, elemental mapping of olfactory bulb sections revealed that 14 days after exposure to γ -Fe₂O₃ (280 ± 80nm), mice brain had on average 31% higher content of Fe compared to the control mice. Synchrotron radiation X-ray fluorescence spectroscopy (SRXRF) mapping confirmed Fe enrichment in deep brain regions of exposed animals, further identified as Fe₂O₃ using K-edge X-ray absorption near edge structure³⁰. Additionally, the same group of researchers evaluated the possibility of two different TiO₂ nanoparticles (80 nm and 155 nm) translocating to the brains of mice after intranasal exposure. Using inductively coupled plasma mass spectrometry (ICP-MS), they found significant increases in Ti content in all brain regions except the hippocampus at all time points (2-, 10-, 20-, and 30-days post-exposure). Surprisingly, the hippocampus exhibited elevated Ti levels at 30 days post-exposure. At that time-point, hippocampus samples had the highest Ti levels compared to others. Pathological changes in cell morphology and pro-inflammatory signalling were observed in cells from the olfactory area and hippocampus post-exposure³¹. Another interesting study involved rats that inhaled poorly soluble manganese salts (MnO, Mn₂O₃) 6 hours per day for 5 days a week. These particles were detected on 6- and 12-days post-exposure in the olfactory bulb and brain structures including midbrain, cerebellum, and frontal cortex. Particles were detected with the graphite absorption spectroscopy of brain tissue samples but were, unfortunately, not imaged so the stronger evidence of particle uptake was not provided in that paper³².

In conclusion, these studies collectively suggest that inhaled nanoparticles can rapidly reach the olfactory region of exposed animals. However, accumulation in deep brain regions appears to be a slower process, taking at least several weeks. This delay is likely attributed to a gradual transport of particles from the nasal cavity and potential entrapment within various cell types along the way, particularly immune cells that seem to be activated after interaction with some nanoparticles. Consequently, it is reasonable to expect that a considerable amount of time, longer than mere days or weeks, would be required for inhaled particles to accumulate in high concentrations within animal brains.

As the literature lacks such long-term in vivo experiments, we aimed to determine the duration it would take for a human exposed to moderately polluted air for 8 hours per day to accumulate 10:1 surface dose, typically used in our experiments. Occupational settings with the highest mean concentrations of PM_{0.1}, such as welding, industrial work, traffic, and restaurants, typically range from 0.7–4.7 × 10⁶ cm⁻³, with the background concentration of 1 × 10⁴ cm⁻³ of air³³. Human respiratory rates fluctuate between 6 liters per minute during rest and 100 liters per minute during vigorous exercise. For activities like light walking at a pace of 5 km h⁻¹, the rate is approximately 25 liters per minute, which we adopted as a representative breathing rate for jobs involving physical exertion³⁴. To ensure a conservative

estimate, we assumed that, under normal breathing conditions, when inhaling air containing $1 \times 10^5 \text{ cm}^{-3}$ particles, only 1% of the inhaled dose translocates further into the brain. This assumption is supported by computational fluid dynamics simulations based on an anatomically accurate model of the human nasal cavity³⁵

The number of particles in the brain after one year of exposure (in mol/L) is thus estimated as:

$$d_{\text{brain}} = \frac{V \times 6.6 \times 10^5 \times PM_{0.1_{\text{occupational}}} \times 0.01}{N_A}$$

Were,

6.6×10^5 is number of minutes in 365 8-hours-long working days

$V_r = 6000 \text{ cm}^3 \text{ min}^{-1}$

$V_w = 25000 \text{ cm}^3 \text{ min}^{-1}$

$V_e = 100000 \text{ cm}^3 \text{ min}^{-1}$

$PM_{0.1_{\text{occupational}}} = 5 \times 10^5 \text{ cm}^{-3}$

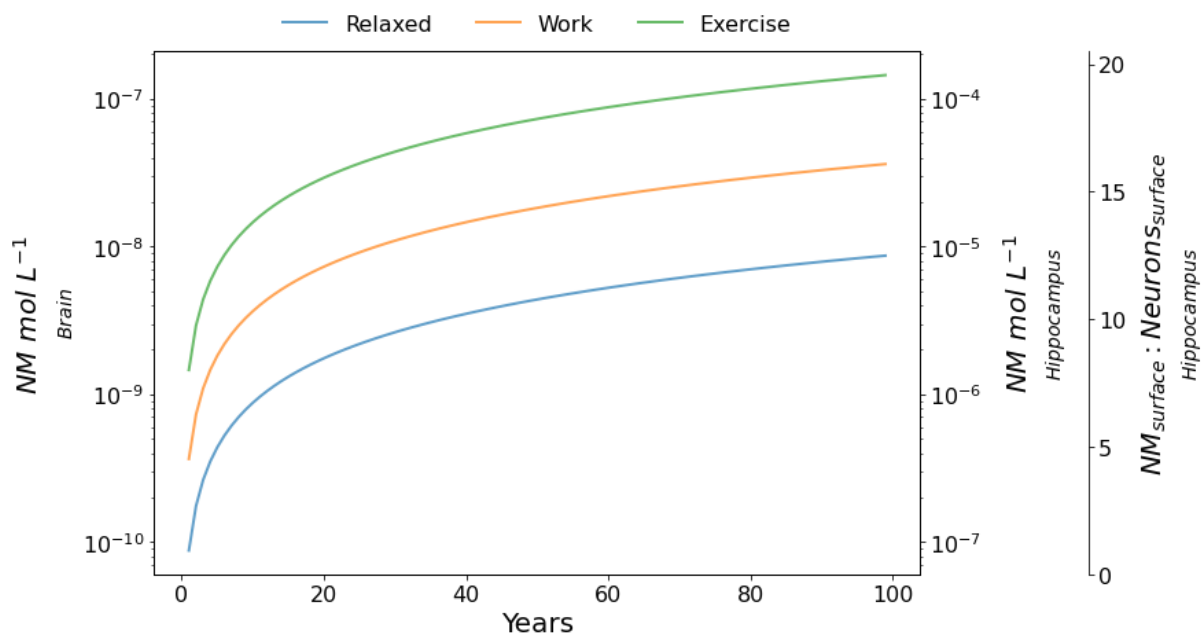
$N_A = 6 \times 10^{23}$

For a particle with dimensions $PM_{\text{dim}} = 100\text{nm} \times 100\text{nm}$, the surface of a single tube is approximately $S_p = a^2 = 1 \times 10^{-10} \text{ cm}^2$.

The overall surface area of neurons has been estimated at 0.34 cm^2 , based on the surface area of the Iqbal 18-well. In a 10:1 surface dose (S_p to S_{neurons}), this corresponds to 3.4 cm^2 of such particles, equivalent to approximately 3×10^{10} tubes or $6 \times 10^{-14} \text{ mol}$. The delivered volume was $3.4 \times 10^{-6} \text{ L}$, resulting in a molar concentration of particles $c = 1.5 \times 10^{-8} \text{ mol L}^{-1}$.

The average volumes of the right and left hippocampus, measured in 24 individuals using T1 oblique slice and three-dimensional MRIs, were 2.90 cm^3 and 2.78 cm^3 , respectively³⁹, resulting in $V_{\text{hippocampus}} \approx 6 \text{ cm}^3 \approx 6 \times 10^{-3} \text{ L}$. The average volume of the human brain (V_{brain}) is approximately $1200 \text{ cm}^3 \approx 1 \text{ L}$ ⁴⁰. This information allowed us to estimate the final particle concentration in the brain and hippocampus for each year of exposure (see figure below).

To fully cover the entire surface of the brain 10 times over, one would need to inhale particles at a concentration of approximately $1 \times 10^{-8} \text{ mol L}^{-1}$, or about 300 times less to achieve the same coverage in the hippocampus.



Based on our estimation, continuous “relaxed-regime” breathing for 60 years, 8 hours each day, in an environment with a particle concentration of $5 \times 10^5 \text{ cm}^{-3}$, would likely lead to an approximate 5:1 surface dose of nanomaterial to the brain. Achieving a 10:1 ratio might not be reached within the life span. In contrast, 25 years of breathing in a “working” regime would result in a 10:1 surface dose, and approximately 5 years under “exercise” breathing regimes would yield a similar level of exposure.

However, for the hippocampus, which requires a dose 300 times lower to achieve a 10:1 surface dose, it would take 35, 10, and 2 years of breathing under the “relaxed,” “working,” and “exercise” regimes, respectively.

Therefore, our calculation suggests that despite the low translocation of inhaled nanoparticles, the cumulative impact of prolonged exposure to polluted air could result in substantial accumulation over the course of several decades. It's worth emphasizing that these timeframes are relevant to the development of neurodegenerative conditions. Furthermore, the hippocampus is connected to the olfactory bulb and is one of the first deep-brain regions that can be exposed to inhaled particles.

7.3 References

1. Kokot, B. *et al.* How to control fluorescent labeling of metal oxide nanoparticles for artefact-free live cell microscopy. *Nanotoxicology* **15**, 1102–1123 (2021).
2. Danielsen, P. H. *et al.* Effects of physicochemical properties of TiO₂ nanomaterials for pulmonary inflammation, acute phase response and alveolar proteinosis in intratracheally exposed mice. *Toxicol. Appl. Pharmacol.* **386**, 114830 (2020).
3. Kozłowski, H., Luczkowski, M., Remelli, M. & Valensin, D. Copper, zinc and iron in neurodegenerative diseases (Alzheimer's, Parkinson's and prion diseases). *Coord. Chem. Rev.* **256**, 2129–2141 (2012).
4. Maynard, C. J., Bush, A. I., Masters, C. L., Cappai, R. & Li, Q.-X. Metals and amyloid- β in Alzheimer's disease. *Int. J. Exp. Pathol.* **86**, 147–159 (2005).
5. Everett, J. *et al.* Biogenic metallic elements in the human brain? *Sci. Adv.* **7**, eabf6707 (2021).
6. Berntsson, E. *et al.* Residue-specific binding of Ni(II) ions influences the structure and aggregation of amyloid beta (A β) peptides. *Sci. Rep.* **13**, 3341 (2023).
7. Lermyte, F. *et al.* Metal Ion Binding to the Amyloid β Monomer Studied by Native Top-Down FTICR Mass Spectrometry. *J. Am. Soc. Mass Spectrom.* **30**, 2123–2134 (2019).
8. Gianoncelli, A. *et al.* Soft X-ray Microscopy Techniques for Medical and Biological Imaging at TwinMic—Elettra. *Appl. Sci.* **11**, 7216 (2021).
9. Gianoncelli, A., Kourousias, G., Merolle, L., Altissimo, M. & Bianco, A. Current status of the TwinMic beamline at Elettra: a soft X-ray transmission and emission microscopy station. *J. Synchrotron Radiat.* **23**, 1526–1537 (2016).
10. Scanning transmission x-ray microscopy with a configurable detector | Applied Physics Letters | AIP Publishing. <https://pubs.aip.org/aip/apl/article-abstract/89/25/251117/921839/Scanning-transmission-x-ray-microscopy-with-a?redirectedFrom=fulltext>.

11. Recent developments at the TwinMic beamline at ELETTRA: an 8 SDD detector setup for low energy X-ray Fluorescence - IOPscience. <https://iopscience.iop.org/article/10.1088/1742-6596/425/18/182001>.
12. A multiplatform code for the analysis of energy-dispersive X-ray fluorescence spectra - ScienceDirect. <https://www.sciencedirect.com/science/article/abs/pii/S0584854706003764>.
13. Kokot, H. *et al.* Prediction of Chronic Inflammation for Inhaled Particles: the Impact of Material Cycling and Quarantining in the Lung Epithelium. *Adv. Mater.* **32**, 2003913 (2020).
14. Peters, R. J. B. *et al.* Silicon dioxide and titanium dioxide particles found in human tissues. *Nanotoxicology* **14**, 420–432 (2020).
15. Peters, R. J. B. *et al.* Characterization of titanium dioxide nanoparticles in food products: analytical methods to define nanoparticles. *J. Agric. Food Chem.* **62**, 6285–6293 (2014).
16. Baj, J. *et al.* Assessment of the Concentration of 51 Elements in the Liver and in Various Parts of the Human Brain—Profiling of the Mineral Status. *Nutrients* **15**, 2799 (2023).
17. Song, B., Liu, J., Feng, X., Wei, L. & Shao, L. A review on potential neurotoxicity of titanium dioxide nanoparticles. *Nanoscale Res. Lett.* **10**, 342 (2015).
18. Ze, Y. *et al.* TiO₂ nanoparticles induced hippocampal neuroinflammation in mice. *PLoS One* **9**, e92230 (2014).
19. Gagnon, J. & Fromm, K. M. Toxicity and Protective Effects of Cerium Oxide Nanoparticles (Nanoceria) Depending on Their Preparation Method, Particle Size, Cell Type, and Exposure Route. *Eur. J. Inorg. Chem.* **2015**, 4510–4517 (2015).
20. Fiorani, L. *et al.* Cerium Oxide Nanoparticles Reduce Microglial Activation and Neurodegenerative Events in Light Damaged Retina. *PLoS One* **10**, e0140387 (2015).
21. Finnegan, M. E. *et al.* Synchrotron XRF imaging of Alzheimer's disease basal ganglia reveals linear dependence of high-field magnetic resonance microscopy on tissue iron concentration. *J. Neurosci. Methods* **319**, 28–39 (2019).

22. Maher, B. A. *et al.* Magnetite pollution nanoparticles in the human brain. *Proc. Natl. Acad. Sci.* **113**, 10797–10801 (2016).
23. Viskup, R., Wolf, C. & Baumgartner, W. Major Chemical Elements in Soot and Particulate Matter Exhaust Emissions Generated from In-Use Diesel Engine Passenger Vehicles. in (2020). doi:10.5772/intechopen.90452.
24. Lippmann, M., Yeates, D. B. & Albert, R. E. Deposition, retention, and clearance of inhaled particles. *Occup. Environ. Med.* **37**, 337–362 (1980).
25. Urbančič, I. *et al.* Nanoparticles Can Wrap Epithelial Cell Membranes and Relocate Them Across the Epithelial Cell Layer. *Nano Lett.* **18**, 5294–5305 (2018).
26. Borgmann-Winter, K. *et al.* Translational potential of olfactory mucosa for the study of neuropsychiatric illness. *Transl. Psychiatry* **5**, e527–e527 (2015).
27. De Lorenzo, A. J. D. The Olfactory Neuron and the Blood-Brain Barrier. in *Ciba Foundation Symposium - Internal Secretions of the Pancreas (Colloquia on Endocrinology)* 151–176 (John Wiley & Sons, Ltd, 1970). doi:10.1002/9780470715369.ch9.
28. Hopkins, L. E. *et al.* Nose-to-brain transport of aerosolised quantum dots following acute exposure. *Nanotoxicology* **8**, 885–893 (2014).
29. Oberdörster, G. *et al.* Translocation of Inhaled Ultrafine Particles to the Brain. *Inhal. Toxicol.* **16**, 437–445 (2004).
30. Wang, B. *et al.* Transport of Intranasally Instilled Fine Fe₂O₃ Particles into the Brain: Micro-distribution, Chemical States, and Histopathological Observation. *Biol. Trace Elem. Res.* **118**, 233–243 (2007).
31. Wang, J. *et al.* Time-dependent translocation and potential impairment on central nervous system by intranasally instilled TiO₂ nanoparticles. *Toxicology* **254**, 82–90 (2008).
32. Elder, A. *et al.* Translocation of Inhaled Ultrafine Manganese Oxide Particles to the Central Nervous System. *Environ. Health Perspect.* **114**, 1172–1178 (2006).

33. Viitanen, A.-K., Uuksulainen, S., Koivisto, A. J., Hämeri, K. & Kauppinen, T. Workplace Measurements of Ultrafine Particles-A Literature Review. *Ann. Work Expo. Health* **61**, 749–758 (2017).
34. Pleil, J. D., Wallace, M. A. G., Davis, M. D. & Matty, C. M. The physics of human breathing: flow, timing, volume, and pressure parameters for normal, on-demand, and ventilator respiration. *J. Breath Res.* **15**, 042002 (2021).
35. Tian, L. *et al.* Correlation of regional deposition dosage for inhaled nanoparticles in human and rat olfactory. *Part. Fibre Toxicol.* **16**, 6 (2019).
36. Honeycutt, N. A. & Smith, C. D. Hippocampal Volume Measurements Using Magnetic Resonance Imaging in Normal Young Adults. *J. Neuroimaging* **5**, 95–100 (1995).
37. Miller, I., Barton, R. & Nunn, C. Quantitative uniqueness of human brain evolution revealed through phylogenetic comparative analysis. *ELife Sci.* **8**, (2019).
38. Baier, P. C. *et al.* Olfactory dysfunction in patients with narcolepsy with cataplexy is restored by intranasal Orexin A (Hypocretin-1). *Brain J. Neurol.* **131**, 2734–2741 (2008).